Nucleic Acids Research, 2025, **53**, gkaf1404
https://doi.org/10.1093/nar/gkaf1404
Gene regulation, Chromatin and Epigenetics

3D enhancer architecture coordinated by CTCF determines immune-related gene expression patterns via RNA polymerase II pause-release in CD4$^+$ T cells

Eun-Chong Lee[1], **Kyungwoo Kim**[1,2], **Sugyung Kim**[1,2], **Mikyoung Kim**[1], **Hyoung-Pyo Kim**[1,2,3,4,*]

[1]Department of Tropical Medicine, Institute of Tropical Medicine, Yonsei University College of Medicine, 50-1 Yonsei-ro, Seodaemun-gu, Seoul 03722, Republic of Korea
[2]Brain Korea 21 PLUS Project for Medical Science, Yonsei University College of Medicine, 50-1 Yonsei-ro, Seodaemun-gu, Seoul 03722, Republic of Korea
[3]Yonsei Genome Center, Yonsei University College of Medicine, 50-1 Yonsei-ro, Seodaemun-gu, Seoul 03722, Republic of Korea
[4]Division of Biology, Pohang University of Science and Technology, Pohang 37673, Republic of Korea

*To whom correspondence should be addressed. Email: kimhp@yuhs.ac

Abstract

CTCF (CCCTC-binding factor) is crucial for organizing mammalian genomes into domains and structural loops, yet its role in enhancer–promoter interactions remains unclear. Here, we demonstrate that 3D enhancer architecture undergoes marked reorganization upon CTCF depletion in activated CD4$^+$ T cells. Despite this, active transcription, particularly driven by STAT5-bound super-enhancers, maintains enhancer loops independently of CTCF. Interestingly, robust enhancer–promoter interactions are associated with the release of RNA polymerase II (RNAPII) pausing and require CTCF-dependent 3D genome organization to shape immune-related gene expression patterns in CD4$^+$ T cells. Notably, CTCF depletion reprograms the transcriptional response of CD4$^+$ T cells to JAK inhibitors by rewiring the STAT5 enhancer network rather than altering the upstream JAK/STAT signaling cascade. This study emphasizes the role of 3D enhancer architecture orchestrated by CTCF and active transcription in directing precise cell identity gene expression through RNAPII pause-release in CD4$^+$ T cells.

Graphical abstract

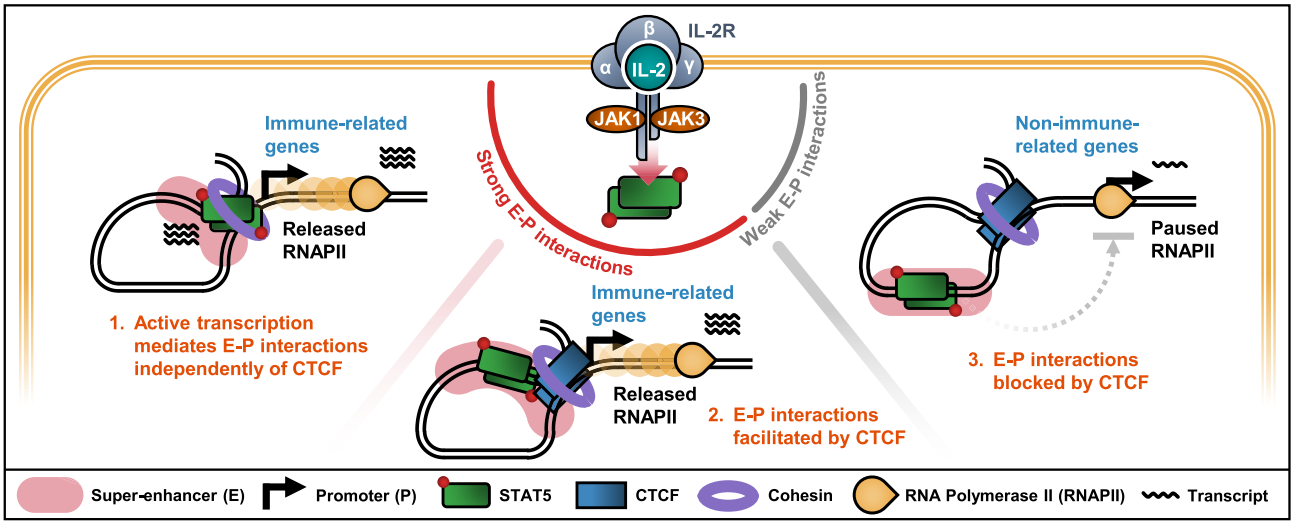

Introduction

The mammalian genome is hierarchically organized within the nucleus, encompassing various levels such as chromosome territories, compartments, and further partitions into topologically associating domains (TADs) and chromatin loops [1]. The formation of TADs and chromatin loops is thought to be mediated by CTCF (CCCTC-binding factor) and cohesin through a loop extrusion mechanism, in which the

Received: November 20, 2024. **Revised:** October 21, 2025. **Accepted:** November 1, 2025

cohesin ring complex slides along the chromatin fiber, extruding a loop until it is blocked by CTCF or other proteins [1]. Most studies have proposed that CTCF binding at the boundaries of TADs creates physically and functionally isolated units in the genome, regulating gene expression by constraining enhancer–promoter interactions within each TAD [2]. Nonetheless, important questions remain about the precise role of CTCF in organizing chromatin loops and forming enhancer networks within TADs, which are essential for coordinated gene transcription [3, 4].

Interleukin-2 (IL-2) functions as the primary growth factor for T lymphocytes and orchestrates the immune response following exposure to antigens [5]. The binding of IL-2 with high affinity ($K_d \approx 10^{-11}$ M) to the trimeric IL-2 receptor (comprising IL-2Rα, IL-2Rβ, and γc) couples with JAK tyrosine kinases and activates the STAT5 transcription factors [5]. Subsequent binding of STAT5 to enhancers triggers critical transcriptional changes that lead to a spectrum of physiological outcomes, including the differentiation and homeostasis of both pro- and anti-inflammatory T cells [5, 6].

In conditional knockout (KO) mice, CTCF in T cells regulates the cell cycle progression of αβ T cells in the thymus and Th2 cytokine gene expression [7, 8]. Moreover, CTCF plays a critical role in shaping the genomic architecture necessary for maintaining $CD8^+$ T cell homeostasis, mediating effector differentiation, and driving early T-cell lineage commitment, while also limiting the formation of memory $CD8^+$ T cells [9–12]. However, how CTCF contributes to integrating external signals such as IL-2 with T-cell-specific gene expression, particularly through 3D enhancer networks, remains poorly understood. To address this, we employed multiple techniques, including H3K27ac HiChIP, *in situ* Hi-C, chromatin immunoprecipitation (ChIP-seq), assay for transposase-accessible chromatin (ATAC-seq), RNA (RNA-seq), and precision nuclear run-on (PRO-seq) sequencing to systematically investigate how CTCF depletion affects enhancer loop formation and transcription in activated $CD4^+$ T cells.

Materials and methods

Mice and cells

Mice carrying a conditional *Ctcf* allele ($CTCF^{fl/fl}$) were crossed with Rosa26-CreER (CreER) mice to generate a tamoxifen-inducible *Ctcf* conditional KO strain (CreER; $CTCF^{fl/fl}$), as described in our previous study [13]. Age- and sex-matched CreER littermate mice were used as wild-type (WT) controls throughout the study. All mouse experimental procedures were approved by the Department of Laboratory Animal Resources Committee of Yonsei University College of Medicine. $CD4^+$ T cells were isolated from mouse spleen by positive selection with the MagniSort™ Mouse CD4 Positive Selection Kit (Thermo Fisher Scientific, 8802-6841-74). Post-sort purity > 85% was assessed using flow cytometry. $CD4^+$ T cells were maintained in RPMI medium supplemented with 10% heat-inactivated fetal bovine serum (Hyclone, SH30071.03), 100 U/ml penicillin/streptomycin (Hyclone, SV30010), and 50 μM 2-mercaptoethanol (Gibco, 21985-023). $CD4^+$ T cells were stimulated with coated αCD3 (2 μg/ml, Biolegend, 100 331) and αCD28 (1 μg/ml, Biolegend, 102 116) in the presence of IL-2 (100 U/ml, Roche, Ro-23-6019) for 6 days. Cells were cultured for 6 days with IL-2 replenishment every 2 days to maintain activation and support survival. Unless otherwise noted, these cells are referred to as 'activated $CD4^+$ T cells' throughout the manuscript. To remove the *Ctcf* allele *in vitro*, 4-OH-tamoxifen (4-OHT; Sigma-Aldrich, H7904) dissolved in 100% ethanol was added on the first day of culture (final 0.5 μM).

RNA extraction and quantitative real-time polymerase chain reaction

$CD4^+$ T cells were subjected to RNA extraction using a Hybrid-R Total RNA kit (GeneAll Biotechnology, 305-101) according to the manufacturer's instructions. RNA was reverse-transcribed using the PrimeScript™ RT Master Mix (Takara Bio, RR036A). The resulting cDNAs were subjected to quantitative real-time polymerase chain reaction (RT-qPCR) using the QuantStudio 3 Real-time PCR System (Applied Biosystems), and the synthesis of double-stranded DNA was monitored during various PCR cycles using the Quanti-Nova SYBR Green PCR Kit (Qiagen, 208 052). The qPCR program was as follows: step 1, 95°C for 2 min; step 2, 95°C for 5 s; step 3, 60°C for 10 s; step 4, return to step 2 and repeat 40 times. At the end of the cycling program, a melting program (from 60 to 95°C with a 0.1°C increment every 1 s) was run to test the specificity of each qPCR. For each sample, duplicate test reactions were analyzed for the expression of the gene of interest, and the results were normalized to *Rpl7* mRNA levels. The primer sequences are listed in Supplementary Table S1. Three to four biological replicates were used for each experiment.

Western blotting

$CD4^+$ T cells were lysed using T-PER™ Tissue Protein Extraction Reagent (Thermo Fisher Scientific, 78 510) with a protease and phosphate inhibitor cocktail (Thermo Fisher Scientific, 78 440). Proteins were separated using 8% sodium dodecyl sulfate–polyacrylamide gel electrophoresis (SDS–PAGE) and transferred to polyvinylidene fluoride membranes. After blocking with 5% skim milk, the membrane was incubated with primary antibodies against α-tubulin (sc32293) from Santa Cruz and CTCF (2899), p-STAT5 (9351), and STAT5 (94 205) from Cell Signaling Technology, followed by incubation with horseradish peroxidase (HRP)-conjugated secondary antibodies, i.e. HPR-linked anti-rabbit IgG (7074) and HPR-linked anti-mouse IgG (7076) from Cell Signaling Technology. The target proteins were visualized using Pierce™ ECL Plus Western Blotting Substrate (Thermo Fisher Scientific, 32 132) and Image Quant LAS 4000 (GE Healthcare). Three biological replicates were used for each experiment.

Flow cytometry

The fluorochrome-conjugated anti-mouse CD4 (GK1.5) antibody was obtained from eBioscience. Cell death and apoptosis were analyzed using the Annexin V Apoptosis Detection Kit (eBioscience, 88-8007-74) according to the manufacturer's protocol. Cell proliferation was determined using a CellTrace™ CFSE Cell Proliferation Kit (Invitrogen, C34554). Stained cells or samples were analyzed by flow cytometry with a FACSVerse system (BD Biosciences) and a FACS LSR Fortessa flow cytometer (BD Biosciences). All flow cytometry data were analyzed using the FlowJo software version 10 (Treestar). Three biological replicates were used for each experiment.

RNA-seq

Strand-specific libraries were generated using the NEBNext® Ultra™ RNA Library Prep Kit for Illumina® (New England Biolabs, E7760) according to the manufacturer's protocol. Barcoded libraries were pooled and sequenced on an Illumina HiSeq platform, generating 100 bp paired-end reads. Three biological replicates were used for each experiment.

ChIP-seq

ChIP-seq was performed as previously described [13]. Briefly, chromatin samples prepared using the appropriate number of fixed cells (5×10^5 for histone modifications and 1×10^7 for transcription factors) were sonicated and subsequently immunoprecipitated with each antibody recognizing CTCF (Cell Signaling Technology, 2899), SMC1A (Bethyl Laboratories, A300-055A), STAT5 (Cell Signaling Technology, 94 205), Phospho-Rpb1 CTD Ser5 (Cell Signaling Technology, 13 523), H3K27ac (Abcam, ab4729), H3K4me1 (Abcam, ab8895), H3K4me3 (Abcam, ab8580), or H3K27me3 (Abcam, ab6002). Antibody–chromatin complexes were captured with Protein A and G Dynabeads (Invitrogen, 100.02D/100.04D) and washed with low-salt wash buffer, high-salt wash buffer, and LiCl wash buffer. Chromatin–antibody complexes immobilized on the magnetic beads were subjected to tagmentation. The eluted DNA was purified using SPRI Ampure XP beads (Beckman Coulter, A63881) and amplified for 8–12 cycles using Nextera PCR primers. Libraries were purified using dual (0.65–0.9×) SPRI Ampure XP beads and paired-end sequenced (100 bp) on an Illumina HiSeq2500 platform. Two biological replicates were used for each experiment.

ATAC-seq

ATAC-seq libraries were prepared as described previously [14]. Briefly, 50 000 cells were pelleted, resuspended in lysis buffer (10 mM Tris, pH 7.4, 10 mM NaCl, 3 mM $MgCl_2$, 0.1% NP-40, 0.1% Tween-20, and 0.01% digitonin) for 10 min on ice and washed with lysis buffer without NP-40 and digitonin. The tagmentation reaction was performed using the Nextera DNA Library Prep Kit (Illumina, FC-121-1030), and the transposed DNA was purified using the MinElute PCR Purification Kit (Qiagen, 28 006). Following PCR amplification using Nextera PCR primers, the libraries were purified using dual (0.5–1.8×) AMPure XP Reagent (Beckman Coulter, A63881) and sequenced on an Illumina HiSeq platform, generating 100 bp paired-end reads. Four biological replicates were used for each experiment.

PRO-seq

PRO-seq experiments were performed as described previously [15] with minor modifications. Briefly, 2×10^6 nuclei were subjected to nuclear run-on at 37°C for 3 min in the presence of 25 μM Biotin-11-CTP (PerkinElmer, NEL542001EA), 0.25 μM CTP, and 125 μM ATP/GTP/UTP (Roche, 11 277 057 001). Total RNA was extracted using TRIzol™ LS Reagent (Invitrogen, 10 296 028) and further fragmented with 0.2 N NaOH on ice for 10 min, and biotinylated nascent RNAs were purified using Dynabeads™ M-270 Streptavidin (Invitrogen, 65 305). Following adaptor ligation, cDNA synthesis, and PCR amplification, the libraries were purified using dual (0.5–1.8×) AMPure XP Reagent (Beckman Coulter, A63881) and sequenced on an Illumina HiSeq platform, generating 100 bp paired-end reads. Two biological replicates were used for each experiment.

In situ Hi-C

In situ Hi-C was performed as previously described [13]. Briefly, 2×10^6 CD4+ T cells were cross-linked with 1% formaldehyde (Sigma, F8775) for 10 min and subsequently quenched with 0.125 M glycine (Duchefa Biochemie, G0709). Chromatin was digested using the MboI restriction enzyme (New England Biolabs, R0147), followed by biotin incorporation using Biotin-14-dATP (Jena Bioscience, NU-835-BIO14-S). After de-cross-linking, the ligated DNA was purified and sheared to 200–300 bp. DNA was purified using a MinElute PCR Purification Kit (Qiagen, 28 006) and quantified using a Qubit dsDNA HS Assay Kit (Invitrogen, Q32854). Subsequently, 150 ng of DNA was used for capture using Dynabeads MyOne Streptavidin C1 (Invitrogen, 65 001), and an appropriate amount of Tn5 enzyme (Illumina, FC-121-1030) was added to the captured DNA to generate the sequencing library. Each library was paired-end sequenced (100 bp) an Illumina NovaSeq6000 platform. Two biological replicates were used for each experiment.

HiChIP

The HiChIP assay was performed as previously described [13]. Briefly, 2×10^6 CD4+ T cells were cross-linked with 1% formaldehyde (Sigma, F8775) for 10 min and subsequently quenched with 0.125 M glycine (Duchefa Biochemie, G0709). Chromatin was digested using the MboI restriction enzyme (New England Biolabs, R0147), followed by biotin incorporation with Biotin-14-dATP (Jena Bioscience, NU-835-BIO14-S) in an end-repair step, ligation, and sonication. The sheared chromatin was incubated with antibodies recognizing H3K27ac (ab4729; Abcam) at 4°C overnight. Chromatin–antibody complexes were captured using Protein A and G magnetic beads (Invitrogen, 100.02D/100.04D) and subsequently washed with low-salt wash buffer, high-salt wash buffer, and LiCl wash buffer before being eluted. DNA was purified using a MinElute PCR Purification Kit (Qiagen, 28 006) and quantified using a Qubit dsDNA HS Assay Kit (Invitrogen, Q32854). Subsequently, 50–150 ng of DNA was used for capture with Dynabeads™ MyOne™ Streptavidin C1 (Invitrogen, 65 001), and an appropriate amount of Tn5 enzyme (Illumina, FC-121-1030) was added to the captured DNA to generate a sequencing library. Each library was paired-end sequenced (100 bp) on an Illumina NovaSeq6000 platform. Two biological replicates were used for each experiment.

RNA-seq data processing

Paired-end sequencing reads were trimmed using Trim Galore (version 0.6.4) with the command-line settings "trim_galore –paired". The trimmed reads were aligned to the mouse mm10 genome assembly using STAR [16] (version 2.6.0a) with the parameters –chimSegmentMin 20 –twopassMode Basic –quantMode TranscriptomeSAM. Gene expression levels were quantified using RSEM [17] (version 1.3.1), with the following parameters: –paired-end –estimated-rspd. Differentially expressed protein-coding genes were determined using the DEseq2 R package [18] (version 1.34.0) with an adjusted *P*-value threshold of 0.05 and a fold change (FC) threshold of 2. For the biological process Gene Ontology (GO) enrich-

ment analysis of the differentially expressed gene symbols, the enrichGO function from the ClusterProfiler [19] R package (version 3.14.3) was utilized, with a *q*-value threshold of 0.05. Strand-specific reads were selected using SAMtools [20] (version 1.9), and normalized using the bamCoverage function from deepTools [21] (version 3.3.0) with the parameter "–normalizeUsing CPM" to generate strand-specific RNA-seq genome track signals.

ChIP-seq data processing

Paired-end sequencing reads were trimmed using Trim Galore with the same parameters as in the RNA-seq analysis and subsequently aligned to the mouse mm10 genome assembly using bwa [22] (version 0.7.12) with default parameter settings. Low-quality reads were removed using SAMtools with the parameters -1 30 –F 1804 –f 2, and duplicate reads were marked using Picard tools (version 2.18.23) with default parameters. Mitochondrial reads and duplicate reads were further removed using SAMtools with the same parameters as previously described. Uniquely mapped reads were normalized using the bamCoverage function from deepTools with command-line option "–normalizeUsing CPM" to generate ChIP-seq genome tracks. ChIP-seq heatmap signals were calculated with the computeMatrix function from deepTools with the command-line options "reference-point –referencePoint center –missingDataAsZero" and additional range information to display normalized read counts near the peak center. Peaks were identified for each sample and biological replicate using MACS2 [23] (version 2.1.2) with command line options "macs2 callpeak -g mm -f BAMPE –nomodel" and input reference data, and additional command line options "-q 0.001″ for H3K27ac ChIP-seq and "–broad" for H3K4me1 and H3K4me3 ChIP-seq. For the H3K27ac ChIP-seq analysis, raw sequencing reads of the replicates were merged and reprocessed as combined results for further analysis. The DESeq2 R package was used to identify differential peaks of ChIP-seq data using read counts from each sample, with customized size factors calculated based on the proportion of uniquely mapped reads between samples, an adjusted *P*-value threshold of 0.05, and an FC threshold of 2.

ATAC-seq data processing

Paired-end sequencing reads were trimmed using Trim Galore, with the same parameters as those used in the RNA-seq analysis. Trimmed reads were mapped to the mouse mm10 reference genome using bowtie2 [24] (version 2.3.2) with the following parameters: –end-to-end –very-sensitive –maxins 2000. Reads with low mapping quality, duplicated reads, and mitochondrial reads were marked and filtered using SAMtools and Picard tools, as in the ChIP-seq analysis. Nucleosome-free regions were selected, and Tn*5* transposase-induced adaptor insertion sites were shifted using the alignmentSieve function from deepTools with the command line-options "–maxFragmentLength 100 –ATACshift." Nucleosome-free region reads were normalized using deepTools, as in the ChIP-seq analysis, to generate ATAC-seq genome tracks. ATAC-seq peak calling was performed using MACS2 with the same parameters as in the ChIP-seq analysis, without using input reference data. The DESeq2 R package was used to identify differentially accessible regions in the ATAC-seq data using the read counts of each sample and customized size factors calculated based on the proportion of nucleosome-free region reads between samples, an adjusted *P*-value threshold of 0.05, and an FC threshold of 2.

PRO-seq data processing

Paired-end sequencing reads were trimmed using Trim Galore, with the same parameters as those used in the RNA-seq analysis. Trimmed reads were mapped to the mouse mm10 reference genome using bwa mem, as in the ChIP-seq analysis. Reads with low mapping quality, duplicated reads, and mitochondrial reads were marked and filtered using SAMtools and Picard tools, as in the ChIP-seq and ATAC-seq analyses. Uniquely mapped reads were normalized using deepTools as in ChIP-seq. Strand-specific reads were selected using SAMtools and normalized using deepTools, as in RNA-seq, to generate strand-specific PRO-seq genome track signals. *De novo* transcript identification was performed using HOMER function findPeaks [25] with the "-style groseq" option for each single and merged samples.

Identification of enhancer RNAs

Enhancer RNAs were identified from PRO-seq data by detecting bidirectional *de novo* transcripts that exhibited overlaps with Pol2S5P ChIP-seq peaks, H3K27ac ChIP-seq peaks, and ATAC-seq peaks, while ensuring they did not overlap with ± 2.5 kb from the transcription start site (TSS) of all genes or the gene body of any protein-coding genes.

In situ Hi-C data analysis

The paired-end read files were processed using HiC-Pro [26] (version 2.11.4). Default settings were used to align reads to the mouse mm10 genome, remove duplicate reads, assign reads to DpnII restriction fragments, filter for valid interactions, and generate binned interaction matrices. After confirming good reproducibility between biological replicates using a hic-spector [27], the replicate data were merged for reprocessing as combined results (Supplementary Table S2). The validated contact pairs were transformed to Juicer .hic files using the hicpro2juicebox function from HiC-Pro with the default parameter settings. To segregate the A and B compartments, eigenvectors for each chromosome of each sample were generated from the Hi-C data using the Juicer tool function eigenvector (version 1.22.01), with KR (Knight–Ruiz) normalization at 100 kb resolution [28]. The Juicer .hic files were converted to .cool files using hic2cool with default parameter options. The compartmentalization strength for KR-normalized Hi-C data at 100 kb resolution was calculated using cooltools [29] (version 0.3.2) and defined as the ratio of (A – A + B – B)/(A – B + B – A) interactions. The insulation score was calculated using an algorithm that aggregated the number of interactions that occurred across chromosome bins and dividing it by the mean number of interactions for the whole chromosome, followed by logarithmization [30]. TAD boundaries were identified using an insulation square analysis algorithm through a matrix2insulation.pl function with parameters -b 500 000 -ids 200 000 -im mean -bmoe 3 -nt 0.1. Intra-TAD DNA interactions, represented as TAD strengths, were calculated using FAN-C [31] (version 0.9.14) with the command-line options "fanc aggregate –tads –expected-norm –log."

HiChIP data analysis

Paired-end read files of the separated and merged samples were processed using HiC-Pro [26], following the same steps as in *in situ* Hi-C analysis (Supplementary Table S3). H3K27ac HiChIP loops were called using FitHiChIP [32] (version 9.0) with 10 kb bin sizes, bias correction by coverage, false discovery rate $< 10^{-5}$, a minimum genomic distance of 20 kb, and a maximum genomic distance of 2 Mb. For identification of loops with differential strength of chromatin interaction, all H3K27ac HiChIP loops with $q < 10^{-5}$ in at least one of the two conditions were compared by applying DESeq2 (version 1.24.0) for the contact counts of each replicate. Gained and lost H3K27ac HiChIP loops were selected using $P < 0.05$ and $\log_2[FC] > 1$ and $\log_2[FC] < -1$, respectively. The cut-off for the super-loops was set to the elbow of the curve, and a tangent line at the cut-off is shown in the graph. The loops below the elbow point of the curve were defined as typical-loops. Super-loops and typical-loops were equally divided into S1, S2, T1, and T2 subgroups based on loop strength.

Aggregated peak analysis

To aggregate genome-wide interaction density near selected loops, the merged HiC and HiChIP matrix dataset was processed using the Juicer tools function apa (version 1.19.02) with command line options "-r 10 000 -k KR -n 30 -w 10." Genome-wide normalized aggregated peak analysis (APA) results were used to plot and calculate the peak to lower left (P2LL) values.

Definition of regulatory elements for annotating HiChIP loop anchors

Promoters were defined as ± 2.5 kb from the TSS of each protein-coding gene. Enhancers were defined as regions with an H3K27ac peak as determined by ChIP-seq. Super-enhancers (SEs) were defined by applying the ROSE algorithm to the H3K27ac peaks with a default stitching size of 12.5 kb [33]. The presence of one or more promoters was considered as a promoter of the HiChIP anchor. The absence of any promoter or enhancer was considered as a non-HiChIP anchor.

Motif enrichment locus overlap analysis

The enrichment of transcription factor motifs within ATAC-seq peaks that overlapped with anchors from each group of HiChIP loops was obtained by BEDTools [34] (version 2.29.2) and analyzed using the "findMotifsGenome.pl" function from HOMER, employing total ATAC-seq peak regions as a background position. For locus overlap analysis (LOLA), ATAC-seq peaks within the region of interest were analyzed using LOLAweb [35] (version 1.4.0) with total ATAC-seq peak regions as background regions and background universe, and compared against the LOLACore region databases for mm10 to identify the enrichment of experimentally derived transcription factor binding locations.

3D clique analysis

3D clique analysis was performed following a previously reported procedure [13]. Briefly, a unidirectional graph of enhancer-centric chromatin interactions was constructed from H3K27ac HiChIP data, where each edge was a significant H3K27ac HiChIP loop, and each vertex was a loop anchor. "3D Cliques" were defined by spectral clustering of the H3K27ac-mediated chromatin interaction using the cluster_louvain function in the igraph R package with default parameters.

Genome editing by ribonucleoprotein electroporation in CD4+ T cells

CD4+ T cells were stimulated with coated αCD3 (2 μg/ml, Biolegend, 100 331) and αCD28 (1 μg/ml, Biolegend, 102 116) in the presence of IL-2 (100 U/ml, Roche, Ro-23-6019) for 2 days before transfection. CRISPR/Cas9 [clustered regularly interspaced palindromic repeats (CRISPR)/CRISPR-associated protein 9] ribonucleoprotein (RNP) complexes containing Alt-R CRISPR/Cas9 guide RNAs (Integrated DNA Technologies, Inc.; Supplementary Table S4) and TrueCut™ Cas9 Protein v2 (Invitrogen, A36496) were delivered into CD4+ T cells using the 4D nucleofector™ platform (Lonza), as described previously [36]. RNPs were formed by adding purified Cas9 protein to single guide RNAs (sgRNAs) in 1 × phosphate-buffered saline (PBS). Complexes were allowed to form for 10 min at room temperature before electroporation. RNP complexes (5 μl) and 1.5 × 10^6 CD4+ T cells (20 μl) were mixed and electroporated according to the manufacturer's specifications using protocol CM137 (P4 primary Cell 4D-Nucleofector™). Electroporated CD4+ T cells were recovered in pre-warmed T-cell media and cultured in the presence of IL-2 (100 U/ml, Roche, Ro-23-6019) for 2 days. To assess genome editing efficiency and confirm STAT5 motif disruption at the targeted enhancer regions (*Dexi* and *Igfbp4* loci), edited genomic regions were PCR-amplified using locus-specific primers (Supplementary Table S1). Indel formation was measured by T7 endonuclease I assay (New England Biolabs, M0302S), and mutations were further validated by Sanger sequencing of PCR products cloned into the TA cloning vector (Takara, 6028), as shown in Supplementary Figs S10 and S11.

Quantification and statistical analysis

The statistical significance of the differences between measurements was determined by the one-sided Wilcoxon rank-sum test (Mann–Whitney U-test) using R, unless otherwise stated. The statistical details of the experiments can be found in the figure legends.

Data visualization

All HiC and HiChIP matrix data were plotted with the HiC-Explorer [37] (version 3.7.2). All ChIP-seq and PRO-seq heat maps, saddle plots, and aggregate plots were generated using the seaborn (version 0.10.1) and matplotlib (version 3.2.1) Python packages. The RNA-seq, ChIP-seq, ATAC-seq, and PRO-seq genome tracks were generated using pyGenomeTracks [38] (version 3.7).

Results

Enhancer loop formation is facilitated by CTCF and active transcription

To decipher the role of CTCF in enhancer loop formation and transcriptional regulation in activated CD4+ T cells,4-OHT was added to CD4+ T-cell cultures on the first day of activation to remove loxP-flanked *Ctcf* alleles in *Ctcf* conditional KO cells (CreER;$CTCF^{fl/fl}$), but not in WT cells

(CreER;CTCF$^{wt/wt}$; Fig. 1A). Depletion of endogenous CTCF in CD4$^+$ T cells was confirmed at the mRNA and protein levels (Supplementary Fig. S1A, B), and CTCF-deficient CD4$^+$ T cells demonstrated slightly increased apoptosis, but relatively similar proliferation, using flow cytometry (Supplementary Fig. S1C, D). Furthermore, the genome-wide occupancy of CTCF and SMC1, measured using ChIP-seq, was considerably reduced by CTCF depletion (Supplementary Fig. S1E–H), and RNA-seq analysis revealed 1 074 deregulated genes (FDR < 0.05, FC > 2.0), of which 660 and 414 were up-regulated and down-regulated, respectively, by CTCF depletion (Supplementary Fig. S1I). Consistent with previous reports using other cell models [13, 39, 40], *in situ* Hi-C analysis demonstrated that CTCF depletion largely maintained compartment organization but disrupted TAD insulation in CD4$^+$ T cells (Supplementary Fig. S2).

We then generated high-resolution contact maps of active enhancers using H3K27ac HiChIP and observed a substantial decrease in the number of HiChIP loops due to CTCF depletion (75 845 in WT and 42 839 in KO; Fig. 1B; Supplementary Fig. S3 for representative contact maps and loop classification strategy). Moreover, most of the HiChIP loops in WT cells were enriched in CTCF, at least in one of the loop anchors (Fig. 1C, D), and half of the loop anchors in WT cells showed CTCF occupancy (Fig. 1E), suggesting an important role for CTCF in the maintenance of enhancer loop formation. HiChIP loops from WT and KO CD4$^+$ T cells were ranked based on loop strength ($-\log_{10}$Q), and super-loops and typical-loops were defined as those above and below the elbow of the loop strength ranking, respectively. Both the super-loops and typical-loops were further evenly divided based on their loop strengths (Fig. 1F). Additional analyses revealed that super-loops tend to span shorter genomic distances than typical-loops, and genes associated with super-loops engage in a greater number of promoter-associated loops in both WT and CTCF-deficient CD4$^+$ T cells (Supplementary Fig. S4). The higher loop strength of the super-loops compared with that of typical-loops was verified by examining *in situ* Hi-C and HiChIP contact counts (Fig. 1G, H).

We examined HiChIP loops, categorized by loop strength, to assess the epigenetic chromatin state and transcriptional activity at their anchors in both WT and CTCF-deficient (KO) CD4$^+$ T cells (Fig. 1I). Super-loops in the WT cells displayed increased CTCF occupancy, providing further insight into the role of CTCF in loop formation. Notably, both WT and KO CD4$^+$ T cells exhibited enhanced occupancy of SMC1A, a cohesin subunit that stabilizes chromatin interactions at the anchors of super-loops. Additionally, the anchors of the super-loops in both WT and KO CD4$^+$ T cells showed reduced enrichment of the repressive histone mark H3K27me3, but higher levels of enrichment for active promoter/enhancer histone marks (H3K27ac, H3K4me1, and H3K4me3), open chromatin regions (ATAC-seq), and active transcription events (PRO-seq and Pol2S5P ChIP-seq; Fig. 1I). When we grouped HiChIP loop anchors from WT CD4$^+$ T cells based on CTCF occupancy at their anchors, a positive correlation was consistently observed between stronger loop formation and epigenetic chromatin states related to active transcription, particularly when CTCF occupancy was absent (Fig. 1J). These findings collectively suggest that CTCF contributes to maintaining enhancer-centric chromatin interactions and that strong transcriptional activity can promote robust enhancer loop formation in the absence of CTCF.

STAT5-bound super-enhancers drive robust enhancer loop formation

We analyzed ATAC-seq peaks at the anchors of enhancer loops to investigate transcription factor binding related to enhancer loop formation. In WT cells, the CTCF motif showed the most enrichment at all loop anchors, regardless of loop strength, highlighting its crucial role in enhancer loop formation (Fig. 2A). By contrast, in CTCF-deficient CD4$^+$ T cells, we observed enrichment of transcription factors related to immune cells, such as NF-κB and ETV4, at the anchors of typical-loops (Fig. 2A). Notably, the STAT5 motif exhibited the highest level of enrichment at the anchors of stronger super-loops (S2) in the KO cells (Fig. 2A). Enrichment of the STAT5 motif was also observed at the S2 loop anchors in WT cells that lacked CTCF occupancy (Supplementary Fig. S5A). The STAT5 signaling pathway appeared to remain active following CTCF depletion, as evidenced by similar levels of STAT5 phosphorylation and genome-wide STAT5 occupancy in KO CD4$^+$ T cells (Fig. 2B, C). Notably, both WT and KO CD4$^+$ T cells showed a more prominent increase in STAT5 ChIP-seq signals at the loop anchors as the loop strength increased, which was particularly significant in KO cells (Fig. 2D) and WT loop anchors lacking CTCF occupancy (Supplementary Fig. S5B). We also noticed a considerable proportion of loop anchors overlapping with STAT5 ChIP-seq peaks as loop strength increased, especially when CTCF was absent (Fig. 2E; Supplementary Fig. S5C).

Given that recent reports have suggested that STAT5 binds to SEs and regulates genes highly induced by IL-2 in mouse T cells [41], we identified SEs using H3K27ac ChIP-seq peaks in WT and KO CD4$^+$ T cells (Fig. 2F; Supplementary Fig. S5D). LOLA of the ATAC-seq peaks within the SEs revealed that sites bound by STAT5 were highly represented in both WT and KO CD4$^+$ T cells (Supplementary Fig. S5E, F), with nearly all SEs displaying STAT5 occupancy (Fig. 2F). Notably, CTCF depletion had minimal effects on H3K27ac enrichment in the SEs (Fig. 2G). Interestingly, we identified an increased overlap of loop anchors with SEs as loop strength increased, with this effect being more pronounced in KO cells than in WT cells (Fig. 2H). These findings collectively illustrate the robust association between STAT5-bound SEs and the formation of strong enhancer loops, particularly in the absence of CTCF. This association was exemplified at the *IL4Ra* and *Cish* loci (Fig. 2I; Supplementary Fig. S5H).

Robust enhancer–promoter interactions are associated with the release of RNA polymerase II pausing

SEs are known for their role in maintaining the high transcriptional output of key cell identity genes [33]. To investigate how SEs activate target genes in CD4$^+$ T cells and the extent to which long-range chromatin interactions play a role in this process, we performed an analysis using H3K27ac HiChIP, which enabled us to identify protein-coding genes that may be regulated by SEs through the formation of enhancer loops (Supplementary Fig. S6A). Genes targeted by SEs exhibited elevated RNA expression levels (Fig. 3A) and a preference for pathways associated with immune cell identity and function in both WT and KO CD4$^+$ T cells (Supplementary Fig. S6B).

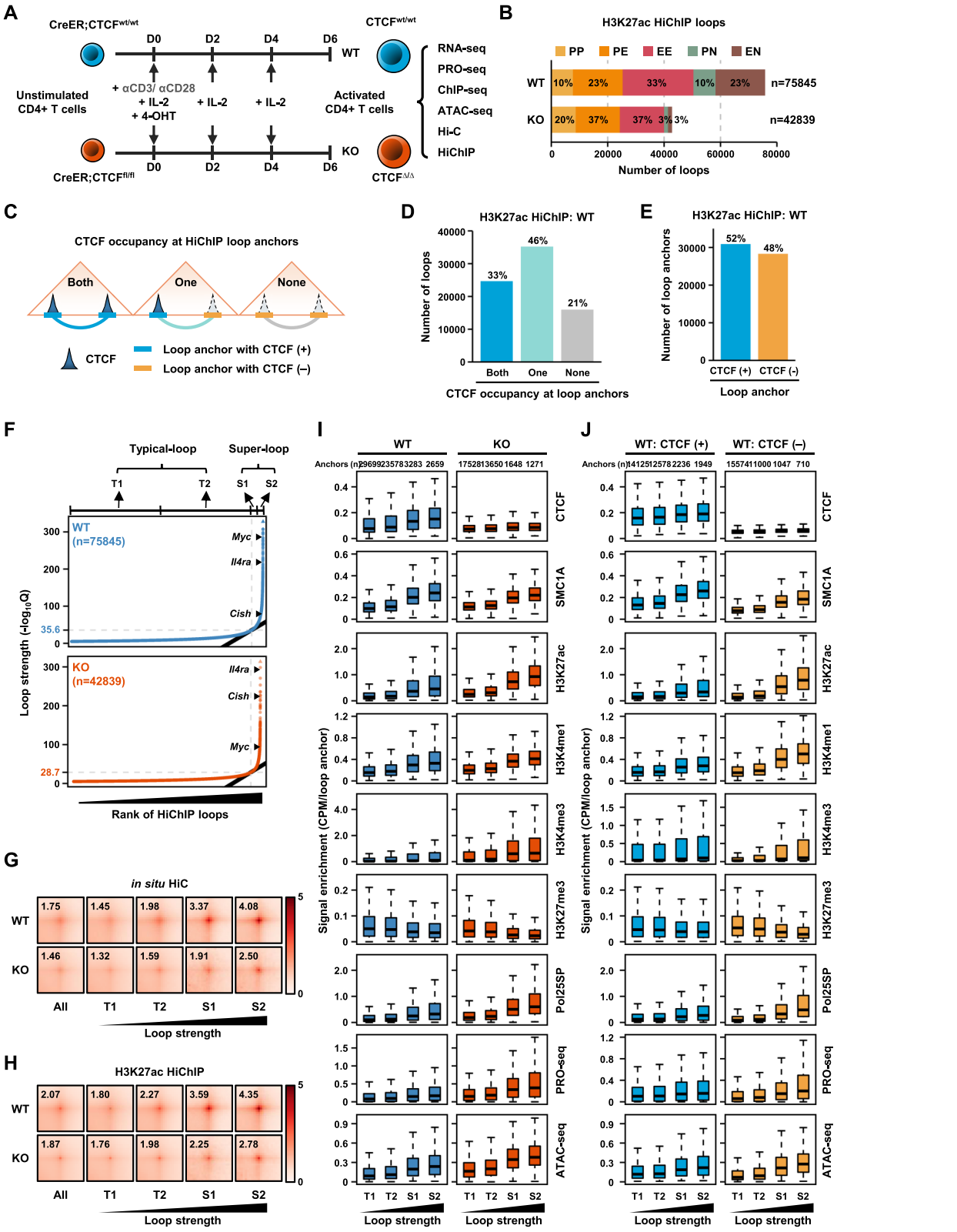

Figure 1. Enhancer loop formation is facilitated by both CTCF and active transcription. (**A**) Schematic depicting the experimental approach employed in this study. (**B**) Distribution of regulatory elements at the anchors of the high-confidence H3K27ac HiChIP loops. (**C**) Three types of H3K27ac HiChIP loops classified based on CTCF occupancy at loop anchors. (**D**) Number of HiChIP loops from WT CD4$^+$ T cells, categorized as described in (C). (**E**) Number of HiChIP loop anchors from WT CD4$^+$ T cells, classified as described in (C). (**F**) The HiChIP loops from WT (top) and KO (bottom) CD4$^+$ T cells were ranked based on their loop strength ($-\log_{10}Q$). Super-loops and typical-loops were defined as those above and below the elbow of the loop strength ranking, respectively. Both super-loops and typical-loops were further divided evenly based on their loop strength. (**G** and **H**) APA of each group of HiChIP loops from WT (top) and KO (bottom) CD4$^+$ T cells was performed by examining *in situ* Hi-C (G) and HiChIP (H) contact counts. (**I**) HiChIP loop anchors from WT (left) and KO (right) CD4$^+$ T cells were examined for enrichment of ChIP-seq, PRO-seq, and ATAC-seq signals. (**J**) HiChIP loop anchors from WT CD4$^+$ T cells, either with (left) or without (right) CTCF occupancy, were examined for enrichment of ChIP-seq, PRO-seq, and ATAC-seq signals. The number of anchors in each group of HiChIP loops was labeled in (I) and (J).

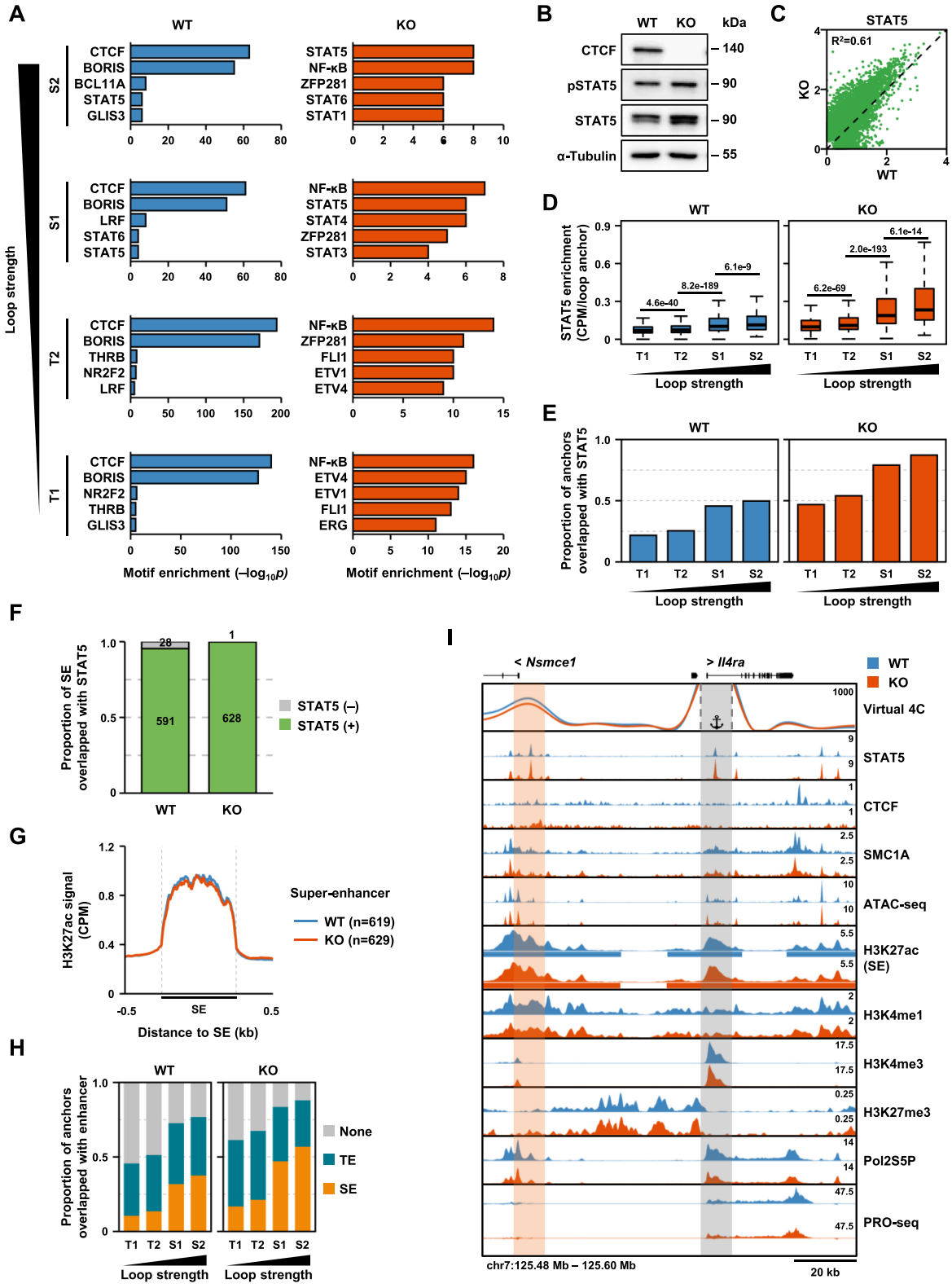

Figure 2. STAT5-bound SEs contribute to the formation of enhancer loops. (**A**) Transcription factor motif identification at ATAC-seq peaks in each group of loop anchors from WT (left) and KO (right) CD4$^+$ T cells. (**B**) Western blotting performed with the indicated antibodies. The data are representative of three independent experiments with similar results. (**C**) Scatter plots of STAT5 ChIP-seq signals from WT and KO CD4$^+$ T cells. (**D**) STAT5 ChIP-seq signals in each group of loop anchors from WT (left) and KO (right) CD4$^+$ T cells. (**E**) STAT5 occupancy in each group of loop anchors from WT (left) and KO (right) CD4$^+$ T cells.(**F**) STAT5 occupancy in SEs. (**G**) ChIP-seq density plots centered around SEs. (**H**) Overlap of SEs or typical-enhancers with each group of loop anchors from WT (left) and KO (right) CD4$^+$ T cells. (**I**) Snapshots displaying virtual 4C (V4C) plots, signal tracks for ChIP-seq, PRO-seq, and ATAC-seq (from top to bottom) at the *Il4ra* locus. The TSS of the *Il4ra* gene is indicated as the viewpoint of V4C.

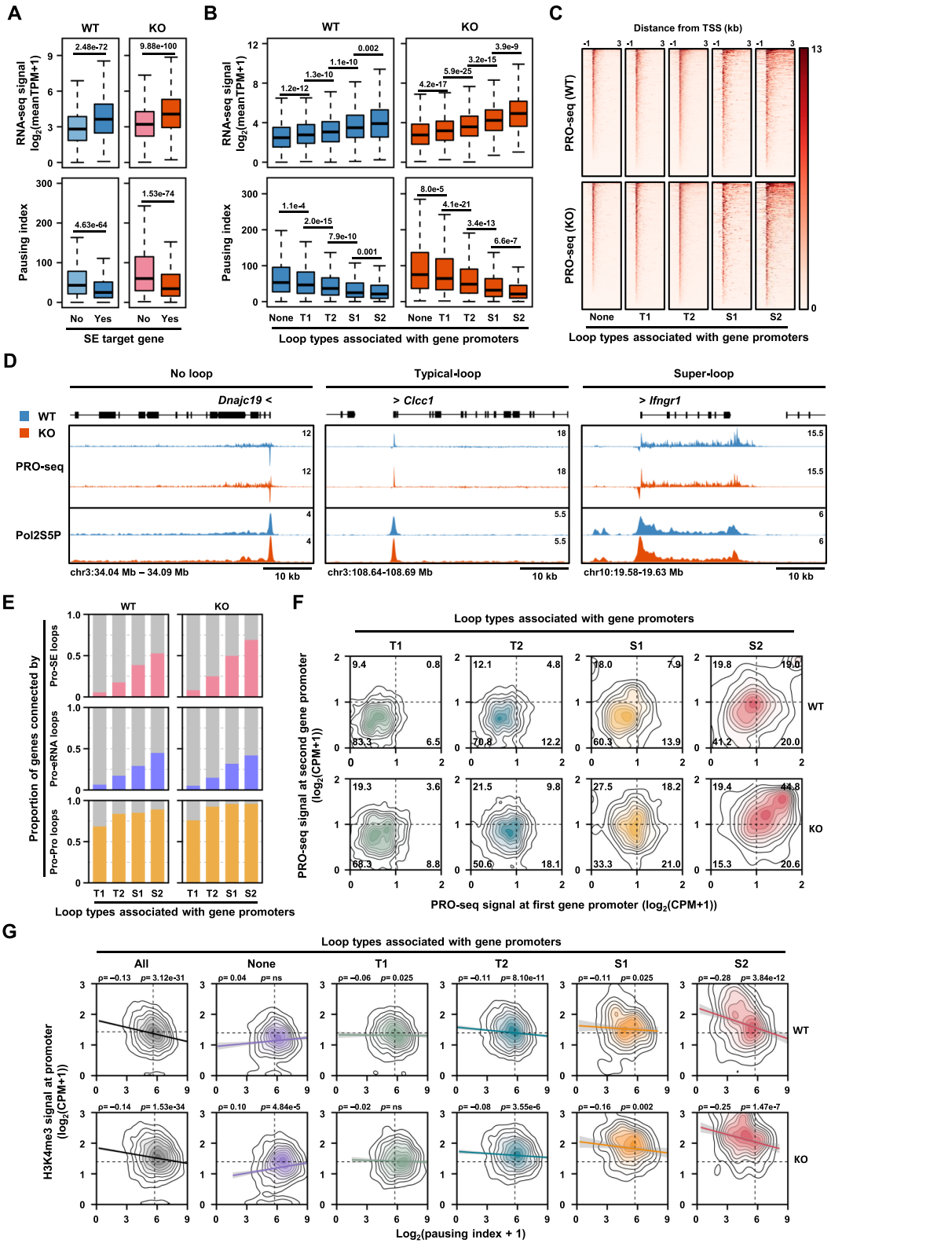

Figure 3. The strength of enhancer–promoter interactions positively correlates with the release of RNA polymerase II (RNAPII) pausing. (**A**) Protein-coding genes, classified by connection to SEs, were examined for RNA expression (top) and pausing index (bottom). (**B**) Protein-coding genes, classified by loop types associated with gene promoters, were examined for RNA expression (top) and pausing index (bottom). (**C**) Heatmaps showing sense-strand PRO-seq reads around TSSs (−1 kb to +3 kb), ranked by decreasing promoter PRO-seq signal. (**D**) Snapshot of signal tracks for PRO-seq and Pol2S5P ChIP-seq in the representative gene regions. (**E**) Proportion of genes with their promoters connected to SEs (top), enhancer RNAs (eRNAs; middle), and promoters of other genes (bottom) within each gene group. (**F**) Correlation analysis between PRO-seq signals at promoters connected by promoter–promoter loops within each gene group. (**G**) Scatter plots showing the correlations between pausing indices and H3K4me3 levels at the promoter regions of each gene group.

Recent studies have suggested that SEs promote high-level gene expression by facilitating the rapid release of transcriptional pausing [42]. Our analysis of the pausing index, based on PRO-seq signals, demonstrated that genes associated with SEs exhibited decreased levels of transcriptional pausing compared with those not associated with SEs (Fig. 3A). Furthermore, when we categorized the protein-coding genes based on their pausing index and conducted GO analysis, we observed that the genes with the lowest levels of transcriptional pausing (Supplementary Fig. S6C) were predominantly associated with immune-related pathways. These results support the notion that SEs play a pivotal role in sustaining the high expression of cell identity genes in $CD4^+$ T cells by promoting the rapid release of transcriptional pausing.

Given the strong link between SEs and robust enhancer loops (Fig. 2H; Supplementary Fig. S5G), we examined whether enhancer loop strength correlated with transcriptional pausing in their target genes. Genes associated with stronger enhancer loops exhibited higher RNA expression and fewer transcriptional pauses (Fig. 3B, C). The rapid release of transcriptional pauses in genes linked to super-loops was further confirmed by analyzing the pausing index based on Pol2S5P ChIP-seq signals (Fig. 3D; Supplementary Fig. S6D, E). Enhancer RNAs (eRNAs) are short, bidirectionally transcribed non-coding RNAs produced at active enhancers, and have been implicated in promoting RNA polymerase II (RNAPII) pause-release [43] (Supplementary Fig. S7). Genes linked to super-loops showed a higher proportion of eRNAs and SEs in the enhancer loop anchors (Fig. 3E). Notably, most protein-coding genes with enhancer loops were connected to other genes via promoter–promoter chromatin interactions (Fig. 3E). Furthermore, both genes connected by promoter–promoter chromatin interactions exhibited a simultaneous increase in nascent RNA expression as the loop strength increased (Fig. 3F). Therefore, active transcription events occurring at distal enhancers, whether involved in the expression of eRNAs or protein-coding genes, are associated with the rapid release of transcriptional pausing through strong enhancer loop formation.

H3K4me3, which is associated with TSSs, regulates RNAPII promoter-proximal pausing, and acute loss of H3K4me3 leads to an increase in RNAPII pausing [44]. All protein-coding genes exhibited a negative correlation between H3K4me3 signals in the promoter regions and the pausing index in both the WT and KO cells (Fig. 3G). Notably, this negative correlation was most pronounced when the genes were connected by strong enhancer loops (S2), whereas it was not observed when they were connected by weaker loops (T1) or not connected (Fig. 3G). These findings collectively emphasize the importance of enhancer loop strength in modulating the release of RNAPII pausing for the expression of cell identity genes in $CD4^+$ T cells.

Robust enhancer–promoter interactions require CTCF to shape immune-related gene expression patterns in $CD4^+$ T cells

We analyzed the extent to which CTCF depletion affected enhancer loop formation, thereby controlling gene expression. Differential loop analyses using H3K27ac HiChIP revealed genome-wide changes in the enhancer loop strength following CTCF depletion, with 10 233 gained loops and 8870 lost loops (Fig. 4A). Our LOLA of the ATAC-seq peaks within the loop anchors revealed a high representation of sites bound by STAT5 in the gained loop anchors (Fig. 4B), which is consistent with the observation that STAT5-bound enhancers contribute to enhancer loop formation in a CTCF-independent manner. However, CTCF sites were highly represented in the lost loop anchors (Fig. 4C), and 93% of the lost loops showed CTCF occupancy in at least one of the loop anchors (Fig. 4D), validating the significant role of CTCF in the maintenance of enhancer loop formation. In contrast, WT loops lacking CTCF binding at both anchors were largely retained following CTCF depletion, suggesting that CTCF-independent enhancer–promoter interactions remain stable and may be regulated by alternative architectural or transcriptional mechanisms (Supplementary Fig. S8). Most of the lost loops were located within the boundaries of WT TADs, whereas 27% of the loops gained in CTCF-deficient $CD4^+$ T cells extended beyond these WT boundaries (Fig. 4E). This observation is consistent with CTCF depletion weakening the insulation capacity at the WT TAD boundaries (Fig. 4F; Supplementary Fig. S2G). Furthermore, the most substantial changes in insulation scores between loop anchors [max (Δ Insulation score)], which reach their peak at WT TAD boundaries (Supplementary Fig. S9A, B), were more pronounced in the gained loops compared with the lost or constant loops (Fig. 4G). Additionally, the number of CTCF peaks between loop anchors, typically highest at the TAD boundaries (Supplementary Fig. S9C), was higher in the gained loops than in the lost or constant loops (Fig. 4H). These findings underscore the role of CTCF as an insulator in both the sub-TAD and TAD scales. Representative genomic loci illustrated the dual function of CTCF in the 3D enhancer network, i.e. maintaining enhancer loop strength at loop anchors and preventing aberrant chromatin interactions through insulation capacity when positioned between them (Supplementary Fig. S9A).

CTCF depletion had a more pronounced impact on the super-loops than on the typical-loops. In WT cells, > 40% of the super-loops displayed reduced chromatin interactions, whereas in KO cells, approximately one-third of the super-loops were newly formed due to enhanced loop strength (Fig. 4I). Furthermore, CTCF depletion had a significant impact on the set of genes connected by super-loops; approximately half of the genes associated with super-loops in WT cells lost their connections (disrupted genes), whereas approximately half of the genes linked with super-loops in KO cells formed new connections following CTCF depletion (acquired genes; Fig. 4J). Genes that maintain their connections with super-loops, even in the absence of CTCF (preserved genes), may be facilitated by the strong transcriptional activity at their loop anchors. Genes connected by super-loops in the WT cells (preserved and disrupted) were primarily associated with immune-related pathways (Fig. 4K). By contrast, genes lacking super-loop connections in the WT cells (acquired and unlinked genes) exhibited a clear preference for pathways related to housekeeping functions, including RNA metabolism (Fig. 4K). This finding suggests that strong enhancer loops are crucial for the expression of cell identity genes, and that CTCF is crucial for the precise alignment of SEs with cell identity genes, thereby preventing aberrant chromatin interactions with non-cell identity genes in $CD4^+$ T cells. Importantly, genes that lost their super-loop connections due to CTCF depletion exhibited a noticeable reduction in RNA expression and an accompanying increase in transcriptional pausing, whereas genes that gained super-loop connections in

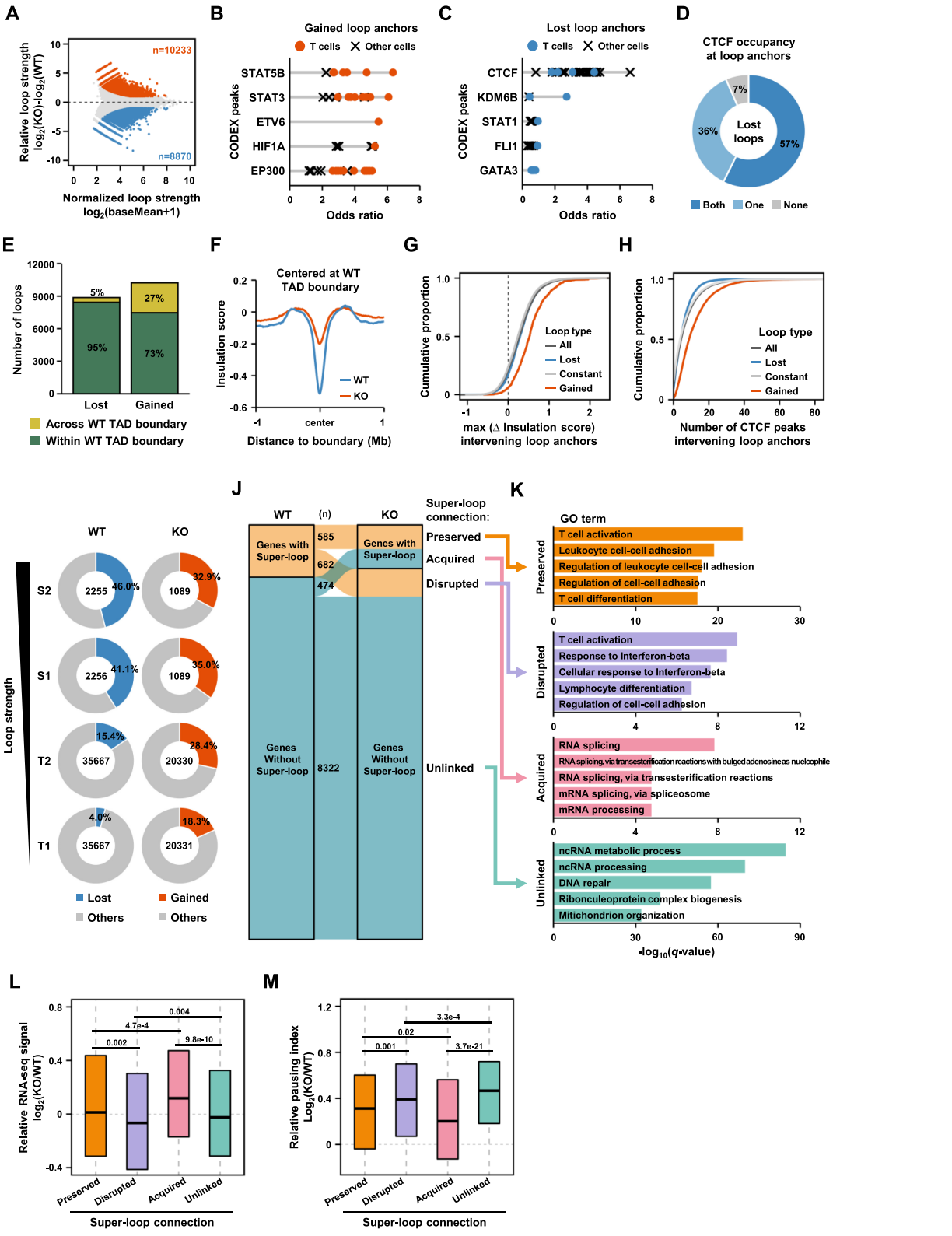

Figure 4. The strength of the enhancer loop contributes to shaping immune-related gene expression patterns. (**A**) MA plot showing significant changes in H3K27ac HiChIP loop strength upon CTCF depletion. The number of loops exhibiting > 2.0-fold increases in WT (blue) or KO (red) CD4+ T cells with a *P*-value < 0.05 is indicated. (**B** and **C**) Relative LOLA enrichment of transcription factors from ATAC-seq peaks at the anchors from gained (B) or lost (C) loops. (**D**) Proportion of anchors of lost loops classified based on CTCF occupancy. (**E**) The number of lost or gained loops, due to CTCF depletion, was categorized as either across WT boundaries or within WT boundaries. (**F**) Genome-wide averaged insulation plotted versus distance around the insulation center at the WT TAD boundary. (**G**) Cumulative proportion of the maximum difference in insulation score observed between loop anchors within each loop type. (**H**) Cumulative proportion of the number of CTCF peaks between loop anchors within each loop type. (**I**) Proportion of lost (left) or gained (right) loops within each loop type. (J–M) Protein-coding genes, classified by changes in super-loop connection to their promoters (**J**), were examined for enrichment of biological process GO terms (**K**), RNA expression (**L**), and pausing index (**M**).

CTCF-deficient cells displayed heightened RNA expression and a decrease in transcriptional pausing (Fig. 4L, M). The intricate interplay between enhancer loop strength and the regulation of transcriptional pausing highlights the pivotal role of the CTCF-dependent 3D chromatin architecture in shaping immune-related gene expression patterns in CD4$^+$ T cells.

CTCF depletion alters the transcriptional response to JAK inhibition by rewiring the STAT5 enhancer network

IL-2 is a well-established critical regulator of immune responses in CD4$^+$ T cells, and IL-2-activated STAT5 facilitates chromatin looping at SEs to preferentially regulate highly inducible immune-related genes [41]. Given that the depletion of CTCF can lead to improper pairing of SEs with their target genes, our subsequent investigation focused on determining the pivotal role of the CTCF-dependent 3D chromatin structure in regulating STAT5-mediated gene expression in CD4$^+$ T cells. The JAK/STAT signaling pathway plays a pivotal role in various cellular processes and modulates the expression of critical mediators associated with cancer and autoimmune diseases [45]. Tofacitinib, the first JAK inhibitor approved for treating rheumatoid arthritis, is recognized for its ability to block the γc cytokine receptor signaling pathway through JAK1 and JAK3 in T cells [46]. We examined whether changes in the 3D chromatin structure induced by CTCF depletion could impact the transcriptional response to JAK inhibitors in activated CD4$^+$ T cells. Combined analysis of STAT5 ChIP-seq and H3K27ac HiChIP demonstrated that almost all gained loops and approximately half of the lost loops exhibited STAT5 occupancy, at least in one of the loop anchors (Fig. 5A), indicating that CTCF depletion significantly rewired the STAT5 enhancer network and its regulation of target genes. Phosphorylation of STAT5 induced by IL-2 was similar between WT and KO cells, but significantly decreased following tofacitinib treatment (Fig. 5B). This treatment resulted in unique genome-wide gene expression patterns that depended on the presence of CTCF (Fig. 5C). To investigate how CTCF depletion altered the transcriptional response to tofacitinib, we identified direct STAT5 target genes displaying reduced RNA expression following tofacitinib treatment through an integrated analysis of STAT5 ChIP-seq, H3K27ac HiChIP, and RNA-seq (Fig. 5D). The majority of tofacitinib-sensitive STAT5 target genes demonstrated chromatin interactions between their promoters and STAT5-bound distal enhancers (Fig. 5D); therefore, we explored two potential regulatory mechanisms by which CTCF depletion affected gene expression through the rewired enhancer network. First, the absence of insulator CTCF led to the formation of chromatin interactions connecting STAT5-bound distal enhancers to target genes, thereby enhancing their expression (Fig. 5E). Second, depletion of CTCF disrupted chromatin interactions between STAT5-bound distal enhancers and target genes, consequently reducing their expression (Fig. 5E). To explore this further, we assessed the changes in the RNA expression of STAT5 target genes following CTCF depletion (Fig. 5F) and their correlation with alterations in chromatin interactions with STAT5-bound distal enhancers (Fig. 5F). Following CTCF depletion, 67 STAT5 target genes were up-regulated, with 51 exhibiting STAT5 loop gains (Fig. 5F), whereas 69 STAT5 target genes were down-regulated, with 15 exhibiting STAT5 loop losses (Fig. 5F; Supplementary Table S5). Following CTCF depletion, modifications in transcriptional pausing were observed concomitant with shifts in the RNA expression of STAT5 target genes. However, this correlation was primarily evident when changes in loop strength occurred between the STAT5-bound distal enhancers and promoters (Fig. 5G). These results demonstrate that CTCF depletion reprograms the transcriptional response of CD4$^+$ T cells to JAK inhibition by rewiring the STAT5 enhancer network rather than by altering the JAK/STAT signaling pathways.

Genome editing validates that the rewired STAT5 enhancer loops alter transcriptional responses to JAK inhibition following CTCF depletion

We used the CRISPR/Cas9 system for genome editing to validate whether the altered transcriptional response to tofacitinib in CTCF-deficient CD4$^+$ T cells was due to the rewiring of the STAT5 enhancer network.

Dexi, which is implicated in the pathogenesis of type 1 diabetes mellitus and autoimmune diseases [47], exhibited a significant increase in chromatin interactions with STAT5-bound SEs following CTCF depletion (Fig. 6A). This interaction resulted in the formation of a super-loop connecting the STAT5-bound SE to the *Dexi* promoter (Fig. 6B), leading to a notable decrease in transcriptional pausing, an increase in *Dexi* expression, and an enhanced transcriptional response to tofacitinib (Fig. 6C–E). Notably, these effects were not observed to the same extent in *Socs1* and *Usp7* (Fig. 6C–E), underscoring the specificity of the regulatory mechanism. We then introduced mutations into the STAT5-binding GAS motifs located in the *Socs1* SE, which showed the most significant changes in chromatin interactions after CTCF depletion, as revealed by V4C (Fig. 6A). Following targeting them with CRISPR/Cas9 in both WT and KO CD4$^+$ T cells, we confirmed the deletion of this element, ΔSTAT5BS, through DNA sequencing (data not shown). In WT cells, deletion of the STAT5-binding GAS motifs did not result in significant changes in the expression of the three genes (Fig. 6F). However, in KO cells, the expression of *Dexi* was significantly reduced by the deletion of the STAT5-binding GAS motifs, whereas *Usp7* and *Socs1* remained unaffected (Fig. 6F). These findings confirm that the reconfiguration of the STAT5 enhancer to the *Dexi* promoter is the primary factor contributing to increased gene expression and tofacitinib sensitivity following CTCF depletion.

Furthermore, our investigation was extended to *Igfbp4*, a key modulator of insulin-like growth factor 1 (IGF1) signaling that is preferentially expressed in murine Th17, Treg, and ILC3 cells [48]. V4C and 3D clique analysis revealed that CTCF depletion selectively disrupted the super-loop connecting the STAT5-bound SE to the *Igfbp4* promoter (Fig. 7A, B), resulting in an increased pausing index and decreased *Igfbp4* RNA expression (Fig. 7C, D). This selective disruption of the super-loop could explain the heightened sensitivity to tofacitinib in *Igfbp4* compared with *Top2a* and *Ccr7* (Fig. 7E). Our genome editing experiments confirmed the direct role of STAT5 located at a distal SE (denoted as ΔSTAT5BS) in controlling *Igfbp4* expression (Fig. 7A, F). Collectively, these findings confirm the pivotal role of the intricate regulatory network orchestrated by 3D genome organization in shaping transcriptional responses to JAK inhibition.

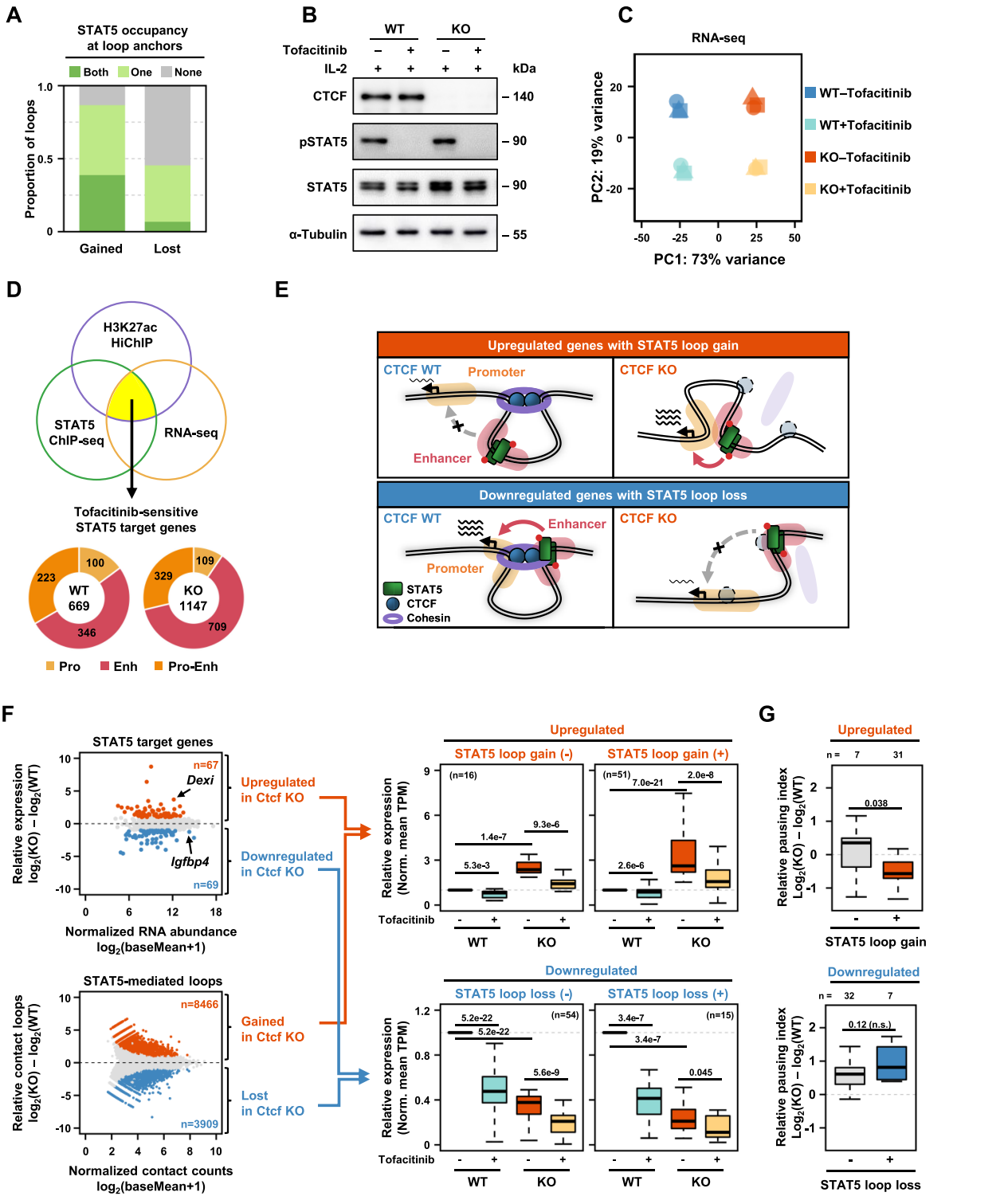

Figure 5. CTCF depletion alters transcriptional response to JAK inhibition by rewiring the STAT5 enhancer network. (**A**) Proportion of anchors of gained or lost loops, classified based on STAT5 occupancy. (**B**) Western blotting performed with the indicated antibodies. The data are representative of three independent experiments with similar results. (**C**) Principal component analysis (PCA) of RNA-seq data. (**D**) Integrated analysis of H3K27ac HiChIP, STAT5 ChIP-seq, and RNA-seq to identify tofacitinib-sensitive STAT5 target genes (top), with the number of genes classified based on the overlap of STAT5 peaks with promoters, distal enhancers, or both (bottom). (**E**) Schematic illustrating the role of CTCF in either blocking (top) or facilitating (bottom) chromatin interactions between promoters and distal STAT5-binding enhancers. (**F**) RNA-seq MA plot showing the differential expression of STAT5 target genes upon CTCF depletion (left top); the number of genes exhibiting > 2.0-fold increases in WT (blue) or KO (red) cells with an FDR < 0.05 is indicated. HiChIP MA plot depicting the changes in STAT5-mediated chromatin interactions upon CTCF depletion (left bottom); the number of loops exhibiting > 2.0-fold increases in WT (blue) or KO (red) cells with an FDR < 0.05 is indicated. Up-regulated genes with a gained STAT5 loop (top right) or down-regulated genes with a lost STAT5 loop (bottom right) upon CTCF depletion were examined for changes in RNA-seq signals by tofacitinib treatment. (**G**) STAT5 target genes, whether up-regulated (top) or down-regulated (bottom), were classified based on the presence of gained (top) or lost (bottom) STAT5 loops and subsequently analyzed for alterations in the pausing index.

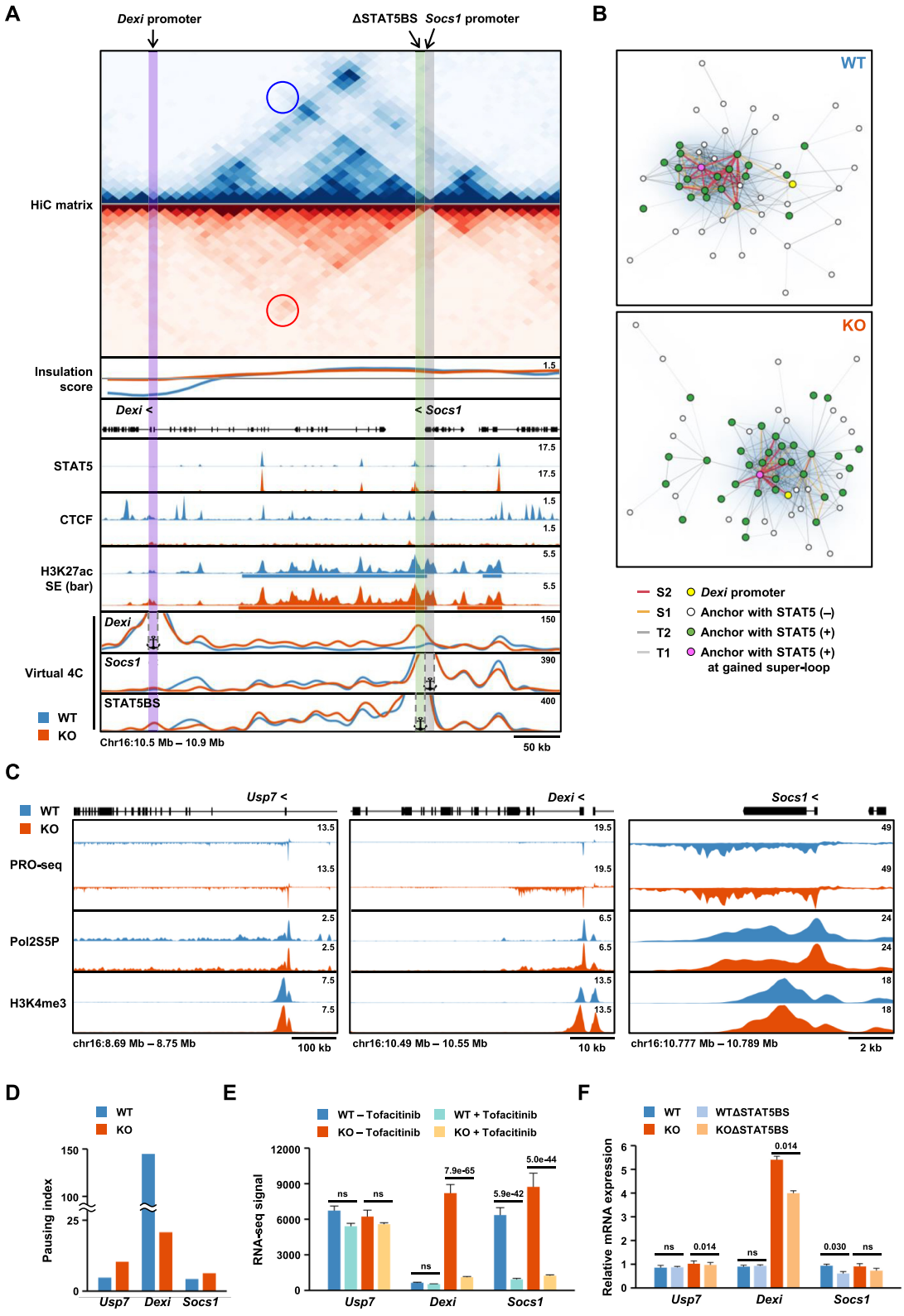

Figure 6. The acquisition of STAT5 enhancer loops following CTCF depletion affects the transcriptional response of the *Dexi* gene to tofacitinib. (**A**) Snapshot displaying the Hi-C contact map, insulation score, ChIP-seq signal tracks for STAT5, CTCF, and H3K27ac, and V4C plots (from top to bottom). Vertical bars highlight the location of viewpoints of V4C analysis. The blue color represents WT and the red color represents KO. (**B**) 3D cliques for *Dexi* loci where each node represented a promoter or an enhancer and each edge represented a significant chromatin interaction of H3K27ac HiChIP loop with $-\log_{10}Q \geq 5$. The color and thickness of each edge indicate the loop type. The color of each node indicates the overlap with STAT5 ChIP-seq peaks. The anchors at gained or lost super-loops are also indicated. (**C**) Snapshot displaying signal tracks for PRO-seq and ChIP-seq for Pol2S5P and H3K4me3 (from top to bottom). (**D**) Changes in pausing indices for the indicated genes upon CTCF depletion. (**E**) Changes in RNA-seq signals for the indicated genes upon CTCF depletion and tofacitinib treatment. (**F**) RT-qPCR analysis for the indicated genes upon CRISPR-mediated mutation of STAT5-binding sites. Four biological replicates with two technical replicates were used for each condition.

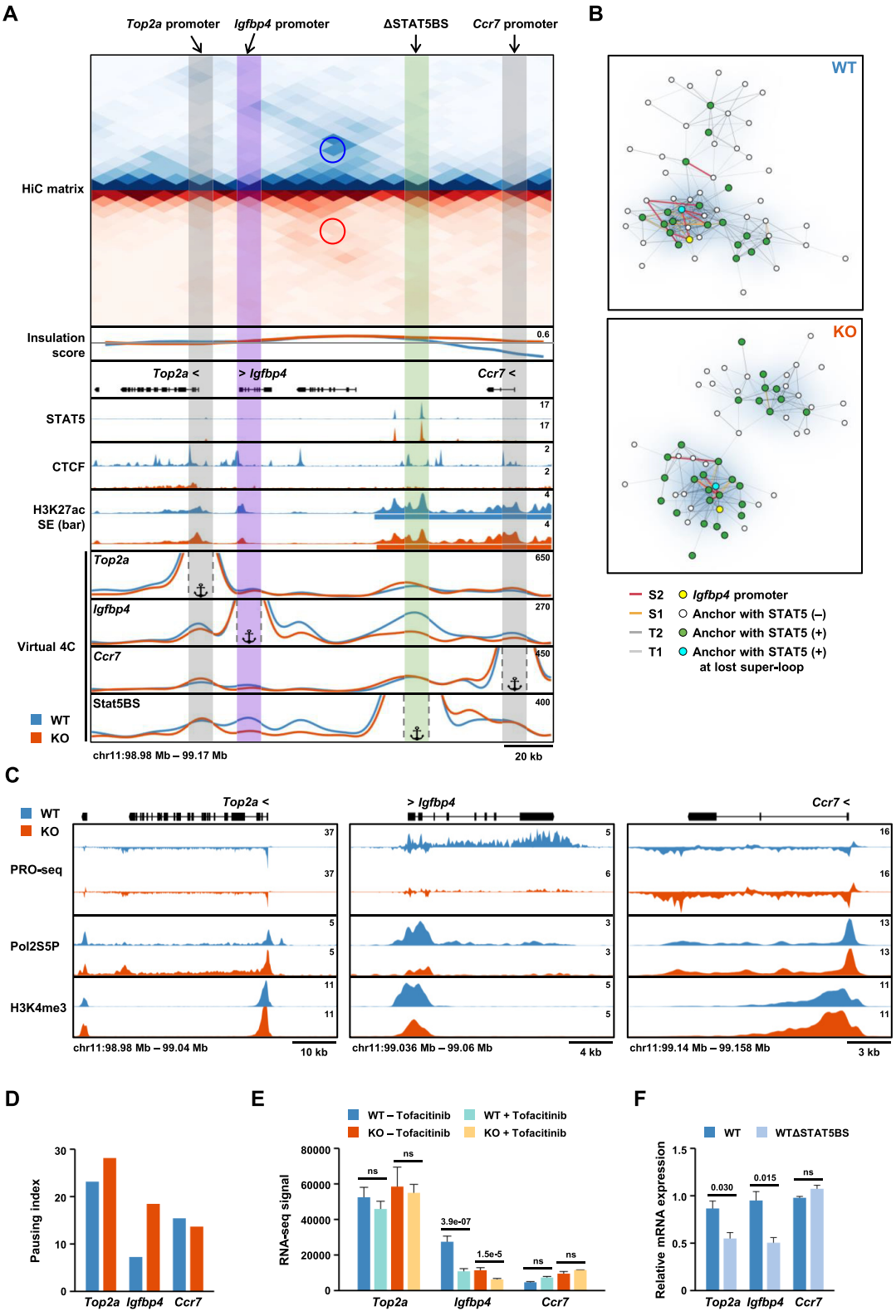

Figure 7. The disruption of STAT5 enhancer loops following CTCF depletion affects the transcriptional response of the *Igfbp4* gene to tofacitinib. (**A**) Snapshot displaying the Hi-C contact map, insulation score, ChIP-seq signal tracks for STAT5, CTCF, and H3K27ac, and V4C plots (from top to bottom). Vertical bars highlight the location of viewpoints of V4C analysis. The blue color represents WT and the red color represents KO. (**B**) 3D cliques for *Igfbp4* loci where each node represented a promoter or an enhancer and each edge represented a significant chromatin interaction of H3K27ac HiChIP loop with $-\log_{10}Q \geq 5$. The color and thickness of each edge indicate the loop type. The color of each node indicates the overlap with STAT5 ChIP-seq peaks. The anchors at lost super-loops are also indicated. (**C**) Snapshot displaying signal tracks for PRO-seq and ChIP-seq for Pol2S5P and H3K4me3 (from top to bottom). (**D**) Changes in pausing indices for the indicated genes upon CTCF depletion. (**E**) Changes in RNA-seq signals for the indicated genes upon CTCF depletion and tofacitinib treatment. (**F**) RT-qPCR analysis for the indicated genes upon CRISPR-mediated mutation of STAT5-binding sites. Four biological replicates with two technical replicates were used for each condition.

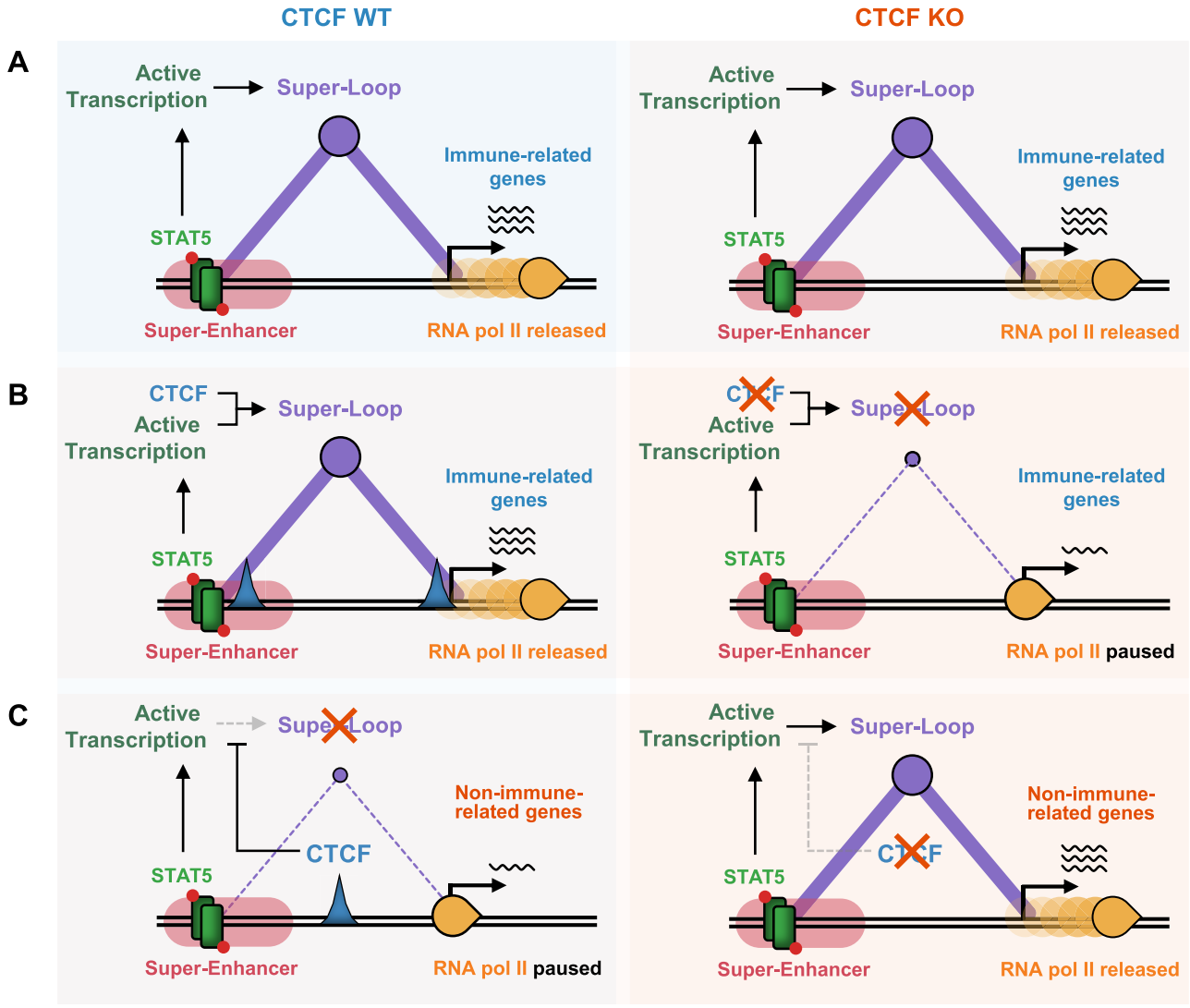

Figure 8. 3D enhancer architecture coordinated by CTCF is associated with modulation of RNAPII pausing and immune-related gene expression in activated CD4$^+$ T cells. In these cells, super-loops can form through active transcription, either independently of CTCF or dependent on it, establishing robust chromatin interactions between STAT5-bound SEs and immune-related genes. These interactions are associated with the release of RNAPII pausing and elevated RNA expression. (**A**) CTCF depletion does not affect the formation of CTCF-independent super-loops, RNAPII pausing, or the expression of their target genes. (**B**) In contrast, CTCF depletion is associated with the disruption of CTCF-dependent super-loops, incomplete RNAPII pause release, and reduced target gene expression. (**C**) As an insulator, CTCF prevents chromatin interactions between STAT5-bound SEs and non-immune-related genes. Upon CTCF loss, these SEs may gain access to non-immune-related genes, which is associated with RNAPII pause-release and increased transcription.

Discussion

Our study demonstrated that CTCF contributes to establishing enhancer loop structures at the sub-TAD scale, supported by marked reorganization of enhancer–promoter chromatin interactions upon depletion of CTCF. However, a notable proportion of enhancer loops persisted in CD4$^+$ T cells lacking CTCF, indicating that alternative barrier proteins for loop extrusion may exist. Additionally, we demonstrate that active transcription, specifically driven by STAT5-bound SEs in activated CD4$^+$ T cells, play a role in shaping enhancer–promoter interactions in a CTCF-independent manner. Considering that many transcription factors and components of the basal transcription machinery contain intrinsically disordered domains, we posit that liquid–liquid phase transitions facilitate the accumulation of RNAPII and other complexes required for gene expression, thereby bridging enhancers to their target promoters over long distances. Further investigations are needed to determine whether the transcription process itself or the resulting transcript contributes to the stabilization of enhancer loop formation, either by impeding the extrusion of chromatin loops driven by the cohesin ring complex or through the assembly of phase-separated transcription condensates.

The pivotal role of enhancers in augmenting transcription rates at target gene promoters is achieved by elevating the local concentration of the transcriptional machinery, facilitating the assembly of the pre-initiation complex, and initiating transcription [49]. However, overcoming RNAPII pausing could represent another common mechanism for enhancer-mediated fine-tuning of transcription, supported by the widespread presence of promoter-proximally paused RNAPII in many transcribed genes [50, 51]. Furthermore, BRD4 and the super elongation complex recruited to enhancers activate pos-

itive transcription elongation factor b (P-TEFb) [52, 53], which phosphorylates negative elongation factor (NELF), DRB sensitivity-inducing factor (DSIF), and Ser2 residues of the RNAPII C-terminal domain (CTD), thereby releasing paused RNAPII into productive transcription elongation [52]. Additionally, the release of paused RNAPII is regulated by enhancer activation via the generation of eRNAs, which interact with and assist in evicting NELF from promoters [43]. Our study demonstrates that enhancers regulate transcription elongation not only through their activity but also via the strength of chromatin interactions with promoters. Specifically, robust enhancer loops, which arise alongside active transcription—with or without CTCF—correlate with reduced RNAPII pausing and increased expression of cell identity genes in CD4+ T cells (Fig. 8). CTCF depletion does not affect the formation of CTCF-independent super-loops (Fig. 8A). However, alterations in enhancer–promoter interactions following CTCF depletion led to changes in gene expression by influencing RNAPII pausing, while causing minimal changes in enhancer activity (Fig. 8B, C). Interestingly, promoters, which can also function as transcriptional enhancers [54], activate nearby promoters by releasing paused RNAPII at target genes in a loop strength-dependent manner. Furthermore, a clear correlation between H3K4me3 and transcriptional pause release was evident only for genes connected by strong enhancer loops, and not for those connected by weaker loops or not connected at all. Overall, our study emphasizes the diverse roles of enhancers in transcriptional regulation and reinforces the idea that enhancers play a direct role in the elongation process.

While our findings reveal robust correlations between enhancer–promoter loop strength and transcriptional activity, several technical and functional factors should be carefully considered. Because HiChIP is a bulk assay, the measured loop strength reflects the cumulative interaction frequency across the cell population. As such, the detected loops may represent contacts that occur in a subset of cells rather than universally. While single-cell 3D genome technologies could in principle address this heterogeneity, current methods remain limited in resolution and coverage, particularly for primary T cells. Despite this, the strong correlation between loop strength and transcriptional output in our data supports the regulatory relevance of the identified interactions.

Although our study clearly demonstrates that CTCF loss perturbs enhancer–promoter communication and transcriptional programs in activated CD4+ T cells, the downstream functional consequences on T-cell effector phenotypes—such as cytokine secretion, activation marker expression, and proliferation under immunological stress—remain to be fully investigated. Furthermore, while this study focuses primarily on chromatin-level and transcriptional changes, future work is needed to determine how STAT5 target gene dysregulation affects immune responses *in vivo*. Such investigations will be essential for understanding how CTCF-dependent genome organization fine-tunes the transcriptional outputs necessary for proper T-cell function and therapeutic modulation.

Aberrant 3D chromatin interactions, which allow cancer cells to exploit otherwise inaccessible SEs and promote their oncogenic behavior, present therapeutic opportunities for clinical treatment [55, 56]. CTCF depletion in CD4+ T cells during IL-2 activation rewires the 3D enhancer network, significantly altering STAT5-mediated gene expression and transcriptional response to a JAK inhibitor, while causing minimal changes in JAK/STAT signaling and SE activities. Despite the relatively stable expression of CTCF, its binding to specific genomic loci is influenced by various factors, including DNA methylation and H3K9me3 [57, 58]. Therefore, in drug development and predicting drug sensitivity, the redistribution of CTCF binding must be considered, as it can alter 3D chromatin structures and affect gene expression.

In summary, the concerted roles of CTCF and active transcription are pivotal for the activation of CD4+ T cells, facilitating the establishment of robust chromatin interactions between STAT5-bound SEs and immune-related genes. This dynamic interplay is associated with strong RNA expression and reduced RNAPII pausing. Furthermore, the significance of a 3D enhancer network emerges as a crucial factor, offering a novel and promising strategy for enhancing disease therapy.

Acknowledgements

Author contributions: Eun-Chong Lee (Data curation [equal], Investigation [lead], Resources [equal], Validation [lead], Visualization [equal], Writing – original draft [lead]), Kyungwoo Kim (Data curation [equal], Formal analysis [equal], Visualization [equal]), Sugyung Kim (Data curation [equal], Formal analysis [equal], Visualization [equal]), Mikyoung Kim (Data curation [equal], Formal analysis [equal], Visualization [equal]), Hyoung-Pyo Kim (Conceptualization [lead], Data curation [equal], Funding acquisition [lead], Project administration [lead], Supervision [lead], Writing – review & editing [lead]).

Supplementary data

Supplementary data is available at NAR online.

Conflict of interest

The authors declare no competing interests.

Funding

The National Research Foundation of Korea (NRF), funded by the Korean government (MSIP) [2020R1A2C2013258, 2022M3A9B6017424, and RS-2025-00562938 to H.-P. Kim].

Data availability

All RNA-seq, ChIP-seq, ATAC-seq, PRO-seq, *in situ* Hi-C, and HiChIP data generated in this study were deposited in the GEO under the accession number GSE243839: https://www.ncbi.nlm.nih.gov/geo/query/acc.cgi?acc=GSE243839.

References

1. Rowley MJ, Corces VG. Organizational principles of 3D genome architecture. *Nat Rev Genet* 2018;19:789–800. https://doi.org/10.1038/s41576-018-0060-8
2. Merkenschlager M, Nora EP. CTCF and cohesin in genome folding and transcriptional gene regulation. *Annu Rev Genom Hum Genet* 2016;17:17–43. https://doi.org/10.1146/annurev-genom-083115-022339
3. Kubo N, Ishii H, Xiong X *et al.* Promoter-proximal CTCF binding promotes distal enhancer-dependent gene activation. *Nat Struct Mol Biol* 2021;28:152–61. https://doi.org/10.1038/s41594-020-00539-5

4. Hsieh TS, Cattoglio C, Slobodyanyuk E *et al.* Enhancer–promoter interactions and transcription are largely maintained upon acute loss of CTCF, cohesin, WAPL or YY1. *Nat Genet* 2022;54:1919–32. https://doi.org/10.1038/s41588-022-01223-8
5. Spolski R, Li P, Leonard WJ. Biology and regulation of IL-2: from molecular mechanisms to human therapy. *Nat Rev Immunol* 2018;18:648–59. https://doi.org/10.1038/s41577-018-0046-y
6. Villarino AV, Kanno Y, O'Shea JJ. Mechanisms and consequences of Jak–STAT signaling in the immune system. *Nat Immunol* 2017;18:374–84. https://doi.org/10.1038/ni.3691
7. Heath H, Ribeiro de Almeida C, Sleutels F *et al.* CTCF regulates cell cycle progression of alphabeta T cells in the thymus. *EMBO J* 2008;27:2839–50. https://doi.org/10.1038/emboj.2008.214
8. Ribeiro de Almeida C, Heath H, Krpic S *et al.* Critical role for the transcription regulator CCCTC-binding factor in the control of Th2 cytokine expression. *J Immunol* 2009;182:999–1010. https://doi.org/10.4049/jimmunol.182.2.999
9. Quon S, Yu B, Russ BE *et al.* DNA architectural protein CTCF facilitates subset-specific chromatin interactions to limit the formation of memory CD8$^+$ T cells. *Immunity* 2023;56:959–78. https://doi.org/10.1016/j.immuni.2023.03.017e910.
10. Liu J, Zhu S, Hu W *et al.* CTCF mediates CD8+ effector differentiation through dynamic redistribution and genomic reorganization. *J Exp Med* 2023;220:e20221288.https://doi.org/10.1084/jem.20221288
11. Hu G, Cui K, Fang D *et al.* Transformation of accessible chromatin and 3D nucleome underlies lineage commitment of early T cells. *Immunity* 2018;48:227–42. https://doi.org/10.1016/j.immuni.2018.01.013
12. Shan Q, Zhu S, Chen X *et al.* Tcf1–CTCF cooperativity shapes genomic architecture to promote CD8$^+$ T cell homeostasis. *Nat Immunol* 2022;23:1222–35. https://doi.org/10.1038/s41590-022-01263-6
13. Yang B, Kim S, Jung WJ *et al.* CTCF controls three-dimensional enhancer network underlying the inflammatory response of bone marrow-derived dendritic cells. *Nat Commun* 2023;14:1277. https://doi.org/10.1038/s41467-023-36948-5
14. Lee EC, Kim K, Jung WJ *et al.* Vorinostat-induced acetylation of RUNX3 reshapes transcriptional profile through long-range enhancer–promoter interactions in natural killer cells. *BMB Rep* 2023;56:398–403. https://doi.org/10.5483/BMBRep.2023-0044
15. Mahat DB, Kwak H, Booth GT *et al.* Base-pair-resolution genome-wide mapping of active RNA polymerases using precision nuclear run-on (PRO-seq). *Nat Protoc* 2016;11:1455–76. https://doi.org/10.1038/nprot.2016.086
16. Dobin A, Davis CA, Schlesinger F *et al.* STAR: ultrafast universal RNA-seq aligner. *Bioinformatics* 2013;29:15–21. https://doi.org/10.1093/bioinformatics/bts635
17. Li B, Dewey CN. RSEM: accurate transcript quantification from RNA-Seq data with or without a reference genome. *BMC Bioinformatics* 2011;12:323. https://doi.org/10.1186/1471-2105-12-323
18. Love MI, Huber W, Anders S. Moderated estimation of fold change and dispersion for RNA-seq data with DESeq2. *Genome Biol* 2014;15:550. https://doi.org/10.1186/s13059-014-0550-8
19. Yu G, Wang LG, Han Y *et al.* clusterProfiler: an R package for comparing biological themes among gene clusters. *Omics* 2012;16:284–7. https://doi.org/10.1089/omi.2011.0118
20. Li H, Handsaker B, Wysoker A *et al.* The Sequence Alignment/Map format and SAMtools. *Bioinformatics* 2009;25:2078–9. https://doi.org/10.1093/bioinformatics/btp352
21. Ramirez F, Dundar F, Diehl S *et al.* deepTools: a flexible platform for exploring deep-sequencing data. *Nucleic Acids Res* 2014;42:W187–91. https://doi.org/10.1093/nar/gku365
22. Li H, Durbin R. Fast and accurate short read alignment with Burrows–Wheeler transform. *Bioinformatics* 2009;25:1754–60. https://doi.org/10.1093/bioinformatics/btp324
23. Zhang Y, Liu T, Meyer CA *et al.* Model-based analysis of ChIP-Seq (MACS). *Genome Biol* 2008;9:R137. https://doi.org/10.1186/gb-2008-9-9-r137
24. Langmead B, Salzberg SL. Fast gapped-read alignment with Bowtie 2. *Nat Methods* 2012;9:357–9. https://doi.org/10.1038/nmeth.1923
25. Heinz S, Benner C, Spann N *et al.* Simple combinations of lineage-determining transcription factors prime cis-regulatory elements required for macrophage and B cell identities. *Mol Cell* 2010;38:576–89. https://doi.org/10.1016/j.molcel.2010.05.004
26. Servant N, Varoquaux N, Lajoie BR *et al.* HiC-Pro: an optimized and flexible pipeline for Hi-C data processing. *Genome Biol* 2015;16:259. https://doi.org/10.1186/s13059-015-0831-x
27. Yan KK, Yardimci GG, Yan C *et al.* HiC-spector: a matrix library for spectral and reproducibility analysis of Hi-C contact maps. *Bioinformatics* 2017;33:2199–201. https://doi.org/10.1093/bioinformatics/btx152
28. Durand NC, Shamim MS, Machol I *et al.* Juicer provides a one-click system for analyzing loop-resolution Hi-C experiments. *Cell Syst* 2016;3:95–8. https://doi.org/10.1016/j.cels.2016.07.002
29. Open2C, Nezar A, Sameer A, Geoffrey F *et al.* Cooltools: enabling high-resolution Hi-C analysis in Python. *PLoS Comput Biol* 2022;20:e1012067. https://doi.org/10.1371/journal.pcbi.1012067
30. Crane E, Bian Q, McCord RP *et al.* Condensin-driven remodelling of X chromosome topology during dosage compensation. *Nature* 2015;523:240–4. https://doi.org/10.1038/nature14450
31. Kruse K, Hug CB, Vaquerizas JM. FAN-C: a feature-rich framework for the analysis and visualisation of chromosome conformation capture data. *Genome Biol* 2020;21:303. https://doi.org/10.1186/s13059-020-02215-9
32. Bhattacharyya S, Chandra V, Vijayanand P *et al.* Identification of significant chromatin contacts from HiChIP data by FitHiChIP. *Nat Commun* 2019;10:4221. https://doi.org/10.1038/s41467-019-11950-y
33. Hnisz D, Abraham BJ, Lee TI *et al.* Super-enhancers in the control of cell identity and disease. *Cell* 2013;155:934–47. https://doi.org/10.1016/j.cell.2013.09.053
34. Quinlan AR, Hall IM. BEDTools: a flexible suite of utilities for comparing genomic features. *Bioinformatics* 2010;26:841–2. https://doi.org/10.1093/bioinformatics/btq033
35. Nagraj VP, Magee NE, Sheffield NC. LOLAweb: a containerized web server for interactive genomic locus overlap enrichment analysis. *Nucleic Acids Res* 2018;46:W194–9. https://doi.org/10.1093/nar/gky464
36. Vakulskas CA, Dever DP, Rettig GR *et al.* A high-fidelity Cas9 mutant delivered as a ribonucleoprotein complex enables efficient gene editing in human hematopoietic stem and progenitor cells. *Nat Med* 2018;24:1216–24. https://doi.org/10.1038/s41591-018-0137-0
37. Ramirez F, Bhardwaj V, Arrigoni L *et al.* High-resolution TADs reveal DNA sequences underlying genome organization in flies. *Nat Commun* 2018;9:189. https://doi.org/10.1038/s41467-017-02525-w
38. Lopez-Delisle L, Rabbani L, Wolff J *et al.* pyGenomeTracks: reproducible plots for multivariate genomic datasets. *Bioinformatics* 2021;37:422–3. https://doi.org/10.1093/bioinformatics/btaa692
39. Nora EP, Goloborodko A, Valton AL *et al.* Targeted degradation of CTCF decouples local insulation of chromosome domains from genomic compartmentalization. *Cell* 2017;169;930–44. https://doi.org/10.1016/j.cell.2017.05.004
40. Lee R, Kang MK, Kim YJ *et al.* CTCF-mediated chromatin looping provides a topological framework for the formation of phase-separated transcriptional condensates. *Nucleic Acids Res* 2022;50:207–26. https://doi.org/10.1093/nar/gkab1242
41. Li P, Mitra S, Spolski R *et al.* STAT5-mediated chromatin interactions in superenhancers activate IL-2 highly inducible genes: functional dissection of the Il2ra gene locus. *Proc Natl Acad Sci*

USA 2017;114:12111–9. https://doi.org/10.1073/pnas.1714019114
42. Henriques T, Scruggs BS, Inouye MO *et al.* Widespread transcriptional pausing and elongation control at enhancers. *Genes Dev* 2018;32:26–41. https://doi.org/10.1101/gad.309351.117
43. Schaukowitch K, Joo JY, Liu X *et al.* Enhancer RNA facilitates NELF release from immediate early genes. *Mol Cell* 2014;56:29–42. https://doi.org/10.1016/j.molcel.2014.08.023
44. Wang H, Fan Z, Shliaha PV *et al.* H3K4me3 regulates RNA polymerase II promoter-proximal pause-release. *Nature* 2023;615:339–48. https://doi.org/10.1038/s41586-023-05780-8
45. Xue C, Yao Q, Gu X *et al.* Evolving cognition of the JAK–STAT signaling pathway: autoimmune disorders and cancer. *Signal Transduct Target Ther* 2023;8:204. https://doi.org/10.1038/s41392-023-01468-7
46. Tanaka Y, Luo Y, O'Shea JJ *et al.* Janus kinase-targeting therapies in rheumatology: a mechanisms-based approach. *Nat Rev Rheumatol* 2022;18:133–45. https://doi.org/10.1038/s41584-021-00726-8
47. Dos Santos RS, Marroqui L, Velayos T *et al.* DEXI, a candidate gene for type 1 diabetes, modulates rat and human pancreatic beta cell inflammation via regulation of the type I IFN/STAT signalling pathway. *Diabetologia* 2019;62:459–72. https://doi.org/10.1007/s00125-018-4782-0
48. DiToro D, Harbour SN, Bando JK *et al.* Insulin-like growth factors are key regulators of T helper 17 regulatory T cell balance in autoimmunity. *Immunity* 2020;52:650–67. https://doi.org/10.1016/j.immuni.2020.03.013
49. Panigrahi A, O'Malley BW. Mechanisms of enhancer action: the known and the unknown. *Genome Biol* 2021;22:108. https://doi.org/10.1186/s13059-021-02322-1
50. Zeitlinger J, Stark A, Kellis M *et al.* RNA polymerase stalling at developmental control genes in the *Drosophila melanogaster* embryo. *Nat Genet* 2007;39:1512–6. https://doi.org/10.1038/ng.2007.26
51. Muse GW, Gilchrist DA, Nechaev S *et al.* RNA polymerase is poised for activation across the genome. *Nat Genet* 2007;39:1507–11. https://doi.org/10.1038/ng.2007.21
52. Chen FX, Smith ER, Shilatifard A. Born to run: control of transcription elongation by RNA polymerase II. *Nat Rev Mol Cell Biol* 2018;19:464–78. https://doi.org/10.1038/s41580-018-0010-5
53. Kanno T, Kanno Y, LeRoy G *et al.* BRD4 assists elongation of both coding and enhancer RNAs by interacting with acetylated histones. *Nat Struct Mol Biol* 2014;21:1047–57. https://doi.org/10.1038/nsmb.2912
54. Li G, Ruan X, Auerbach RK *et al.* Extensive promoter-centered chromatin interactions provide a topological basis for transcription regulation. *Cell* 2012;148:84–98. https://doi.org/10.1016/j.cell.2011.12.014
55. Zhuang HH, Qu Q, Teng XQ *et al.* Superenhancers as master gene regulators and novel therapeutic targets in brain tumors. *Exp Mol Med* 2023;55:290–303. https://doi.org/10.1038/s12276-023-00934-0
56. Jia Y, Chng WJ, Zhou J. Super-enhancers: critical roles and therapeutic targets in hematologic malignancies. *J Hematol Oncol* 2019;12:77. https://doi.org/10.1186/s13045-019-0757-y
57. Wang H, Maurano MT, Qu H *et al.* Widespread plasticity in CTCF occupancy linked to DNA methylation. *Genome Res* 2012;22:1680–8. https://doi.org/10.1101/gr.136101.111
58. Tam PLF, Cheung MF, Chan LY *et al.* Cell-type differential targeting of SETDB1 prevents aberrant CTCF binding, chromatin looping, and cis-regulatory interactions. *Nat Commun* 2024;15:15. https://doi.org/10.1038/s41467-023-44578-0

Received: November 20, 2024. **Revised:** October 21, 2025. **Accepted:** November 1, 2025